Journal of the Brazilian Society of Mechanical Sciences and Engineering (2018) 40:70
https://doi.org/10.1007/s40430-017-0933-3

TECHNICAL PAPER

On the development of a higher order time-domain Rankine panel method for linear and weakly non-linear seakeeping computations

Felipe Ruggeri[1] · **Rafael A. Watai**[1] · **Claudio M. P. Sampaio**[1] · **Alexandre N. Simos**[1]

Received: 16 May 2017 / Accepted: 13 December 2017 / Published online: 23 January 2018

Abstract

The development of a numerical method for the computation of the linear and weakly non-linear wave effects on floating bodies is presented. The method is formulated in terms of a higher order time-domain boundary elements method based on the Rankine sources. The higher order approach is assumed for both body geometry (using NURBS) and computed function (using B-splines), the former in a standard CAD geometry format to provide more flexibility. In this paper, the procedures adopted for the numerical solution of the main mathematical problems involved are thoroughly described and discussed, with the purpose of documenting important aspects of these methods that are often absent in the literature. Several verification cases are presented, including first-order quantities (motion RAOs, velocity field, and free-surface elevation) and second-order loads (mean drift, sum, and difference components). Regarding the latter, at the present stage of the development, the numerical method is able to compute the so-called quadratic components of forces and moments. For these loads, steady-state solutions in both monochromatic and bichromatic waves are compared to the results obtained with a well-known frequency-domain code.

Keywords Higher order boundary element method · Time-domain · Rankine sources · Seakeeping · Quadratic second-order loads.

1 Introduction

Computational solution of diffraction–radiation wave effects on floating bodies through boundary element methods (BEM) has been performed for more than 40 years, during which many academic and commercial codes have been presented. Some of these codes are nowadays widespread and frequently used by the offshore industry in the design and analysis of fixed and floating units. Linear frequency-domain codes appeared first, mainly due to the limitations imposed by the computing power available at the time. Some examples, among many others, are the codes AQWA [1], WAMIT [31], AEGIR [29, 30], LAMP [32–34], and NEMOH [2]. More recently, several new codes have been developed based on a time-domain approach, both with academic and commercial purposes, see, for instance, SeaFEM [4]. Nonetheless, most of these codes are not open source, rendering the integration with other numerical codes infeasible.

Several studies have been performed in the last years for the simulation of non-linear waves and strongly non-linear wave–body interaction in Numerical Wave Tanks (NWT). For instance,Grilli et al. [15] and Grilli and Subramanya [13, 14] investigated strongly non-linear waves in a 2D approach using a higher order scheme, the latter including wave breaking phenomenon, which was extended to 3D problems in Grilli et al. [16, 17]. van Daalen [7] formulated a fully non-linear time-domain BEM for the evaluation of the 2D wave-maker problem, forced oscillation tests, and decay tests. Ferrant [9, 10] and Ferrant et al. [11] have employed higher order boundary element methods to simulate fully non-linear diffraction problems in regular and irregular waves. Tanizawa et al. [50, 51], Koo [27], Koo and Kim [26, 28] applied the bidimensional fully non-linear approach for the evaluation of response to waves of floating bodies in a numerical wave tank simulation. Contento [5] has also studied the fully non-linear problem

---

Technical Editor: Celso Kazuyuki Morooka.

✉ Felipe Ruggeri
felipe.ruggeri@gmail.com

[1] Numerical Offshore Tank (TPN), University of São Paulo, Prof. Luciano Gualberto Av, 380, São Paulo, Brazil

validating his results initially with Vugts [53] experiments for forced oscillation and then performing decay tests and simulations of motion response to waves. Xue et al. [58], Wu [57], and Yan [59] have evaluated 3D non-linear steep waves applying the fully non-linear approach, which was extended to wave–body interactions in [35]. Greco [12] has applied a 2D non-linear wave model for the investigation of green water phenomenon, including additional effects like hydroelasticity. Dombre et al. [8] solved the free floating wave–structure interaction based on a fully non-linear potential flow solver for a rectangular cylinder, extending the method presented in Guerber et al. [18] for a fully submerged circular cylinder.

The Numerical Offshore Tank group of the University of São Paulo (TPN-USP) has been developing since 2000 a Dynamic Simulator (Dynasim) in cooperation with Petrobras (see, for instance, Nishimoto et al. [41]), for which the main goal is to predict the behavior of offshore platforms under the combined action of waves, current and wind. Dynamic analysis including floating units, moorings, and risers is performed in a coupled approach.

The present version of Dynasim computes the floating body motions using pre-computed hydrodynamic coefficients from a frequency-domain analysis and Cummins [6] equation. This is certainly a common approach for this kind of analysis, but it is not free of problems, as, for example, the numerical difficulties that arise in the computation of the memory functions, mainly when resonant effects are present (e.g., in moonpools or during side-by-side operations, etc.). Furthermore, treating problem that involve multiple bodies and changes in their relative positions becomes quite cumbersome. The considerations above motivated the development of a Rankine Panel Method, which has begun with a linear 2D-code Ruggeri [45], later extended to the 3D case using a low-order approach concerning both body geometry and computed functions Watai [55]. Nonetheless, it is known that a low-order approach is not the most appropriate for the computation of mean, slow, and sum drift forces and also wave–current interaction loads, for they all require accurate computation of the derivatives of the velocity potential. Therefore, for the development of the code reported in this paper, which aims at progressively including such non-linear effects, a higher order approach was adopted for both geometry and velocity potential.

Previous comparisons regarding computational time and accuracy for the lower and higher order approaches were provided by Liu et al. [36] that applied quadratic quadrilateral elements (eight nodes) and by Maniar [39], that applied a B-spline description, both works dealing only with frequency-domain solutions. Liu et al [37] computed the mean-drift forces and wave run-up using the quadratic elements in combination with the wave source Green function [56] on the ISSC TLP to avoid the need for free-surface discretization. The results obtained regarding the body velocity on a sphere in uniform flow were computed using the quadratic element derivatives and compared to analytical solution. Prins [44] also studied the first- and second-order (mean drift) loads with and without current assuming a low-order approach, computing the velocity field using a finite-difference scheme. Liu et al. [38] computed the mean and double-frequency quantities in frequency domain, which required the free-surface discretization in the inner region to solve the second-order free-surface condition, a procedure similar to the one that is also adopted by WAMIT [54].

More recently, Kim and Kim [24] extended the method for wave–current interaction using the nine-node quadratic elements for both potential function and body geometry. Rankine source was employed as Green function; thus, also the free surface was discretized. Shao [47] also applied a similar approach using 12-node cubic polynomial for both potential function and geometry in the study of first- and second-order quantities, both in the presence and in the absence of a small current.

In the pursuit of a time-domain HOBEM code, many different alternatives are in principle available for the solution of the various computations that must be performed. The upsides and disadvantages of each alternative, however, are often disputable and frequently important details regarding the algorithms required to perform such computations are absent in the specialized literature. For the code developer, this situation certainly makes his task substantially harder. Having this observation in mind, a detailed description of some important algorithms that are critical to the performance of the code will be presented along the present text, as a comparison of the numerical results for a simplified flow (hemisphere under uniform current) changing the collocation points distribution to verify the best option.

Furthermore, before the code is applied to more complex problems involving real offshore systems and operations, a thorough verification of the computations is required. In this paper, some first- and second-order wave–structure computations concerning a hemisphere are presented to provide a better comprehension of the numerical results. However, the second-order wave forces are evaluated considering only the quadratic interactions of zeroth/first-order quantities; thus, the second-order potential is not solved in the present method. Although the extension to the full second-order solution is certainly envisaged, it involves a much more complex solution which drastically increases the demanding in terms of mathematical processing and computational time. From a practical point of view, this approach is sufficient for a proper estimation of the low-frequency forces for many applications, particularly, for slender structures that involve low diffraction effects, such as semi-submersible units [40].

In the time-domain simulations, care was taken to guarantee that transient effects had effectively vanished during the simulation period, so that a proper analysis of the steady-state solution could be performed. With this approach, the second-order loads in monochromatic and bichromatic waves are compared with the results obtained from the frequency-domain code WAMIT [54] v6.4. Some preliminary results regarding the present method can be seen in Ruggeri et al. [46].

2 First-order problem

The mathematical problem is formulated considering floating or fixed structures under the incidence of gravity waves, neglecting current effects. The flow is assumed irrotational and incompressible and the free surface is described by a single-valued mathematical function, thus restricting the solution to non-overturning waves only.

The weakly non-linear formulation assumes all quantities described by Stokes series, see, for instance, Eq. (1), which are replaced in the conventional no-flux condition for the fixed and floating bodies and in the free-surface conditions. Following the conventional procedure, all the quantities are expanded using Taylor series about the mean-wetted surfaces [22, 23], where $\varepsilon = H/\lambda$ is the wave steepness (H wave height, λ wavelength). The no-flux conditions expanded in Taylor series and combined to Stokes' one can be seen in Eq. (3), where the zeroth-order potential is null in the absence of current and $\mathbf{V}_Q^{(1)}$ is the first-order boundary velocity in point Q (here, $\bar{S}$ denotes the flow boundaries):

$$\varphi = \varphi^{(0)} + \sum_{i=1}^{\infty} \varphi^{(i)}(t) \cdot \varepsilon^i \tag{1}$$

$$\frac{\partial \varphi}{\partial t} = \sum_{i=1}^{\infty} \frac{\partial \varphi^{(i)}(t)}{\partial t} \cdot \varepsilon^i \tag{2}$$

$$\nabla \varphi_Q^{(1)} \cdot \mathbf{n}_Q^{(0)} + \nabla \varphi_Q^{(0)} \cdot \mathbf{n}_Q^{(1)} + \nabla[(\mathbf{x}_Q^{(1)} \cdot \nabla) \varphi_Q^{(0)}] \cdot \mathbf{n}_Q^{(0)} = \mathbf{V}_Q^{(1)} \cdot \mathbf{n}_Q^{(0)}, \; Q \in \bar{S}. \tag{3}$$

With the purpose of ensuring stability of the time-domain simulations, an approach that makes use of the so-called acceleration potential [time derivative of the potential function, as shown in Eq. (2)] is adopted, as previously proposed by van Daalen [7], Tanizawa [49], and Bandyk and Beck [3]. The total velocity and acceleration potentials are then decomposed into two different quantities representing the incident and "disturbed" wave field (Eq. (4)), in which the latter includes all the radiation and diffraction effects (added mass forces, potential damping, excitation forces, etc.). One will readily notice that this procedure differs from the traditional frequency-domain approach, in which the total potential is decomposed in seven or eight components. The proposed decomposition allows for an easier introduction of non-linear effects in the future, for instance, those associated with moving meshes in time-domain simulations, as presented in [55]:

$$\varphi^{(1)} = \phi_I^{(1)} + \phi_S^{(1)}. \tag{4}$$

The first-order problem concerning the velocity potential can be described as solving Laplace's equation (6) considering the boundary conditions in Eqs. (7) and (8), which are essentially no-flux conditions, in the mean-wetted fixed ($\bar{S}_{\mathrm{fixed}}$), prescribed motion ($\bar{S}_{\mathrm{pm}}$), and floating bodies ($\bar{S}_{\mathrm{fb}}$). Here, g is the gravity acceleration; $\phi_I^{(1)}$ is the first-order incident wave field (Eq. (5)) for finite water depth assuming the superposition of several regular components with amplitude A_i, wave frequency ω_i, wave number k_i, incoming wave direction β_i (measured from the x-axis in the counter-clockwise) and relative phase δ_i; $(V_G^{(1)}; \omega^{(1)})$ denotes the first-order body velocity vector. Examples of fixed surfaces are the bottom, walls, and bottom mounted surfaces, while examples of prescribed motion surfaces are wave makers, bodies on forced motion oscillation tests etc. A simplified setup that illustrates a numerical wave tank can be seen in Fig. 1 (the coordinate axis is right-hand oriented with the y-axis perpendicular to the xz plane.), considering the instantaneous and mean-wetted surfaces. It should be reminded that only the mean surfaces are considered in the numerical computations:

$$\phi_I^{(1)} = \sum_{i=1}^{N} \frac{\zeta_i g}{\omega_i} \frac{\cosh k_i(z+h)}{\cosh k_i h} \cos (k_i x \cos \beta_i + k_i y \sin \beta_i - \omega_i t + \delta_i) \tag{5}$$

$$\nabla^2 \phi_S^{(1)} = 0 \quad \text{in} \quad \bar{\Omega} \tag{6}$$

$$\frac{\partial \phi_{S_Q}^{(1)}}{\partial n_Q^{(0)}} = -\frac{\partial \phi_{I_Q}^{(1)}}{\partial n_Q^{(0)}}, \qquad Q \in \bar{S}_{\mathrm{fixed}} \tag{7}$$

$$\frac{\partial \phi_{S_Q}^{(1)}}{\partial n_Q^{(0)}} = [\mathbf{n}_Q^{(0)}, (Q^{(0)} - G^{(0)}) \wedge \mathbf{n}_Q^{(0)}] \cdot \{\mathbf{v}_G^{(1)}, \omega^{(1)}\} - \frac{\partial \phi_{I_Q}^{(1)}}{\partial n_Q^{(0)}}, \qquad Q \in \{\bar{S}_{\mathrm{pm}} \cup \bar{S}_{\mathrm{fb}}\}. \tag{8}$$

The boundary conditions in the fixed and prescribed motion boundaries are always known, while the floating body condition requires the computation of body motions, which is performed solving Eq. (9) for the first-order problem, where $\mathbf{n}$ is the normal vector components (n_x, n_y, and n_z); $[M]$, $[C^{(0)}]$, and $[K^{(0)}]$ are the mass, external damping, and total stiffness matrices

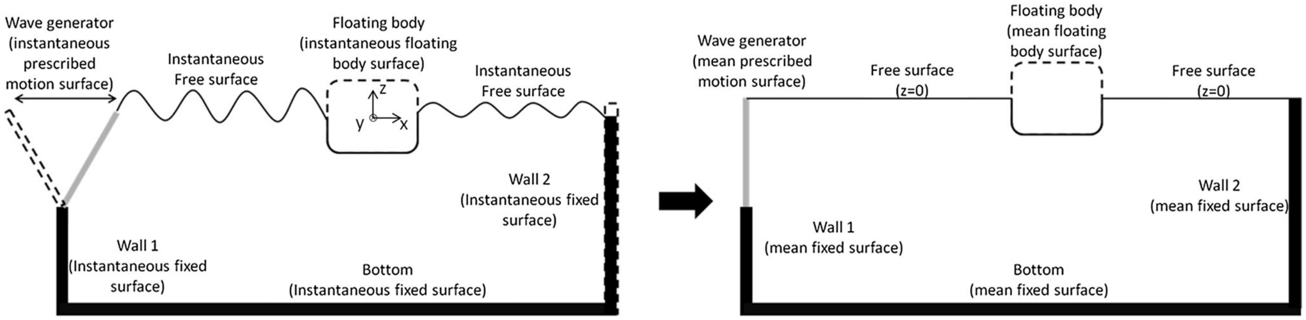

Fig. 1 Sketch of the boundary surfaces (left— instantaneous one, right—the mean surfaces) (Please note that the figure provides only a schematic representation of a 2D section of the tank, since the computational model adopted is three dimensions)

(hydrostatic + external), respectively. It should be noticed that in this formulation, the mass and damping matrices represent only the physical body mass and external viscous damping, since the potential effects are taken into account directly in the pressure integration, including the relative phases effects regarding added mass/potential damping:

$$[M]\{\ddot{X}^{(1)}\} + [C^{(0)}]\{\dot{X}^{(1)}\} + [K^{(0)}]\{X^{(1)}\} = -\rho \iint_{\bar{S}_{\mathrm{fb}}} \left[\frac{\partial \phi^{(1)}_{S_Q}}{\partial t} + \frac{\partial \phi^{(1)}_{I_Q}}{\partial t}\right] \left\{\begin{matrix} \mathbf{n}^{(0)}_Q \\ (Q^{(0)} - G^{(0)}) \wedge \mathbf{n}^{(0)}_Q \end{matrix}\right\} \mathrm{d}S_Q \tag{9}$$

The first-order body motions are defined by $\{X^{(1)}\}$ and velocities by $\{\dot{X}^{(1)}\}$, which considers the first-order velocity of the center of gravity $\mathbf{v_G}^{(1)}$ in the translational degrees of freedom (DoF) and $\omega^{(1)}$ for the rotational ones. The normal vector is also decomposed assuming Stokes series; thus, $\mathbf{n}^{(0)}$ corresponds to the normal vector of the mean surfaces.

The boundary conditions in the free surface include the dynamic (10) and kinematic (11) equations. Here, they are not combined into a single one for convenience of the numerical implementation and to allow flexibility for future inclusions of non-linear effects. The last terms presented in both equations represent a sponge layer that is applied to replace the conventional radiation conditions in the outer boundaries of the computational domain; see, for instance, Israeli and Orszag [21]:

$$\frac{\partial \phi^{(1)}_S}{\partial t} + g\eta^{(1)}_S + v\phi^{(1)} = 0, \quad z = 0 \tag{10}$$

$$\frac{\partial \eta^{(1)}_S}{\partial t} - \frac{\partial \phi^{(1)}_S}{\partial z} + v\eta^{(1)} = 0, \quad z = 0 \tag{11}$$

where the damping function $v(x, y)$ is defined in Eq. (12), where a and b are constants, λ is the largest expected wavelength, ω is the respective wave frequency, and d_{beach} is the length of the damping zone. More details concerning the sponge layer approach assumed can be seen in [45, 55]:

$$v(x, y) = a\omega \left(\frac{[x^2 + y^2]^{1/2} - d_{\mathrm{beach}}}{b\lambda} \right)^2. \tag{12}$$

The simulation of bodies that are fixed or undergo prescribed motions is easier, since the motions (positions, velocities, and accelerations) are already known regardless the hydrodynamic pressure acting on the body surface, which may then be computed using a conventional backward difference scheme. On the other hand, the velocity and acceleration of a floating body are unknown prior to the solution of the body motion's equation (9) and this fact may lead to instability of the numerical method. For avoiding this problem, an additional BVP is solved for the acceleration potential, allowing the computation of the time derivative of the potential function more accurately than if solving a backward finite-difference scheme. The BVP problem for the acceleration potential involves solving Laplace's equation (13) with the boundary conditions (14) and (15) in $\bar{S}_{\mathrm{fixed}}$, $\bar{S}_{\mathrm{pm}}$, and $\bar{S}_{\mathrm{fb}}$:

$$\nabla^2 \left(\frac{\partial \phi^{(1)}_S}{\partial t} \right) = 0, \quad \text{in} \quad \bar{\Omega} \tag{13}$$

$$\frac{\partial^2 \phi^{(1)}_{S_Q}}{\partial n^{(0)}_Q \partial t} = -\frac{\partial^2 \phi^{(1)}_{I_Q}}{\partial n^{(0)}_Q \partial t}, \quad Q \in \bar{S}_{\mathrm{fixed}} \tag{14}$$

$$\frac{\partial^2 \phi^{(1)}_{S_Q}}{\partial n^{(0)}_Q \partial t} = [\mathbf{n}^{(0)}_Q, (Q^{(0)} - G^{(0)}) \wedge \mathbf{n}^{(0)}_Q] \cdot \{\mathbf{a}^{(1)}_G, \dot{\omega}^{(1)}\} - \frac{\partial^2 \phi^{(1)}_{I_Q}}{\partial n^{(0)}_Q \partial t}, \quad Q \in \{\bar{S}_{\mathrm{pm}} \cup \bar{S}_{\mathrm{fb}}\}. \tag{15}$$

It should be noticed that the dependence on the acceleration can be eliminated from the floating body boundary condition using Eq. (16), where $\{\mathbf{n}^{*(0)}_Q\} = \{\mathbf{n}^{(0)}_Q, (Q^{(0)} - G^{(0)}) \wedge \mathbf{n}^{(0)}_Q\}$. ***Therefore, the only variable that needs to be solved on the floating body surfaces is the time derivative of the potential function:

$$
\begin{aligned}
&\{\ddot{X}^{(1)}\} \cdot \{\mathbf{n}_Q^{*(0)}\}^T = -\rho[M]^{-1} \iint_{\bar{S}_{\mathrm{fb}}} \frac{\partial \phi_{S_Q}^{(1)}}{\partial t} \{\mathbf{n}_Q^{*(0)}\} \cdot \\
&\{\mathbf{n}_Q^{*(0)}\}^T \mathrm{d}S_Q \quad + -\rho[M]^{-1} \iint_{\bar{S}_{\mathrm{fb}}} \frac{\partial \phi_{I_Q}^{(1)}}{\partial t} \{\mathbf{n}_Q^{*(0)}\} \cdot \\
&\{\mathbf{n}_Q^{*(0)}\}^T \mathrm{d}S_Q - [C^{(0)}]\{\dot{X}^{(1)}\} \cdot \{\mathbf{n}_Q^{*(0)}\}^T \\
&- [K^{(0)}]\{X^{(1)}\} \cdot \{\mathbf{n}_Q^{*(0)}\}^T.
\end{aligned} \tag{16}
$$

The mathematical problem is solved by applying Green's identity (Eqs. (17) and (18)), considering the Rankine sources as Green function. As a consequence, no boundary condition is automatically satisfied. In the present method, the points selected for the solution of the integral equation are located in continuous regions; thus, the contribution of the solid angle will be always 2π regardless the geometry discretization, as discussed next:

$$
\begin{aligned}
&\iint_{\partial\Omega_{-P}} \left(\varphi_Q \frac{\partial G_{PQ}}{\partial n_Q} - G_{PQ} \frac{\partial \varphi_Q}{\partial n_Q} \right) \mathrm{d}\partial\Omega_Q \\
&= \begin{cases} -4\pi\varphi_P, \text{ if } P \text{ inside } \Omega \\ -2\pi\varphi_P, \text{ if } P \text{ at } \partial\Omega \\ 0, \text{ if } P \text{ outside } \Omega \end{cases}
\end{aligned} \tag{17}
$$

$$
\begin{aligned}
&\iint_{\partial\Omega_{-P}} \left(\frac{\partial \varphi_Q}{\partial t} \frac{\partial G_{PQ}}{\partial n_Q} - G_{PQ} \frac{\partial^2 \varphi_Q}{\partial t \partial n_Q} \right) \mathrm{d}\partial\Omega_Q \\
&= \begin{cases} -4\pi \dfrac{\partial \varphi_P}{\partial t}, \text{ if } P \text{ inside } \Omega \\ -2\pi \dfrac{\partial \varphi_P}{\partial t}, \text{ if } P \text{ at } \partial\Omega \\ 0, \text{ if } P \text{ outside } \Omega. \end{cases}
\end{aligned} \tag{18}
$$

The boundary integral equations that arise when considering the boundary conditions ($\frac{\partial \varphi_Q}{\partial n_Q}, \frac{\partial^2 \varphi_Q}{\partial t \partial n_Q}$) are given by Eqs. (19) and (20), which are obtained by replacing the boundary conditions (7) and (8) into (17) for the velocity potential and (14), (15) and (16) into (18) for the acceleration potential equation. As already mentioned, the acceleration in the boundary conditions of floating bodies can be eliminated using the motion equation (9), providing a direct computation of the time derivative of the first-order potential without the need for computing the acceleration in the boundary. The substitution leads to Eq. (21) and the term containing the time derivative of the first-order potential can be grouped to the dipole term in the left side of the linear system. This procedure leads to a stable condition for the time-domain simulation, for it couples the flow acceleration to the body motions.

The solution of the integral equations is performed using a panel method that assumes a higher order approach for both geometry and velocity potential. The geometry is described in a NURBS format, which is standard in the CAD field:

$$
\begin{aligned}
&2\pi\phi_{S_P}^{(1)} + \iint_{\bar{S}_{\mathrm{fixed}}} \phi_{S_Q}^{(1)} \frac{\partial}{\partial n_Q^{(0)}} \left(\frac{1}{r_{PQ}} \right) \mathrm{d}S_Q \\
&+ \iint_{\bar{S}_{\mathrm{pm}}} \phi_{S_Q}^{(1)} \frac{\partial}{\partial n_Q^{(0)}} \left(\frac{1}{r_{PQ}} \right) \mathrm{d}S_Q \\
&+ \iint_{\bar{S}_{\mathrm{fb}}} \phi_{S_Q}^{(1)} \frac{\partial}{\partial n_Q^{(0)}} \left(\frac{1}{r_{PQ}} \right) \mathrm{d}S_Q \\
&- \iint_{\bar{S}_{\mathrm{fs}}} \frac{\partial \phi_{S_Q}^{(1)}}{\partial z} \left(\frac{1}{r_{PQ}} \right) \mathrm{d}S_Q \\
&\quad = -\iint_{\bar{S}_{\mathrm{fixed}} \cup \bar{S}_{\mathrm{pm}} \cup \bar{S}_{\mathrm{fb}}} \frac{\partial \phi_{I_Q}^{(1)}}{\partial n_Q^{(0)}} \left(\frac{1}{r_{PQ}} \right) \mathrm{d}S_Q + \{\dot{X}^{(1)}\}_{\mathrm{pm}} \cdot \\
&\left[\iint_{\bar{S}_{\mathrm{pm}}} \left(\frac{1}{r_{PQ}} \right) \{\mathbf{n}_Q^{*(0)}\} \mathrm{d}S_Q \right] \\
&+ \{\dot{X}^{(1)}\}_{\mathrm{fb}} \cdot \left[\iint_{\bar{S}_{\mathrm{fb}}} \left(\frac{1}{r_{PQ}} \right) \{\mathbf{n}_Q^{*(0)}\} \mathrm{d}S_Q \right] \\
&- \iint_{\bar{S}_{\mathrm{fs}}} \phi_{S_Q}^{(1)} \frac{\partial}{\partial n_Q^{(0)}} \left(\frac{1}{r_{PQ}} \right) \mathrm{d}S_Q
\end{aligned} \tag{19}
$$

$$
\begin{aligned}
&2\pi \frac{\partial \phi_{S_P}^{(1)}}{\partial t} + \iint_{\bar{S}_{\mathrm{fixed}}} \frac{\partial \phi_{S_Q}^{(1)}}{\partial t} \frac{\partial}{\partial n_Q^{(0)}} \left(\frac{1}{r_{PQ}} \right) \mathrm{d}S_Q \\
&+ \iint_{\bar{S}_{\mathrm{pm}}} \frac{\partial \phi_{S_Q}^{(1)}}{\partial t} \frac{\partial}{\partial n_Q^{(0)}} \left(\frac{1}{r_{PQ}} \right) \mathrm{d}S_Q \\
&+ \iint_{\bar{S}_{\mathrm{fb}}} \frac{\partial \phi_{S_Q}^{(1)}}{\partial t} \frac{\partial}{\partial n_Q^{(0)}} \left(\frac{1}{r_{PQ}} \right) \mathrm{d}S_Q - \iint_{\bar{S}_{\mathrm{fs}}} \frac{\partial^2 \phi_{S_Q}^{(1)}}{\partial t \partial z} \left(\frac{1}{r_{PQ}} \right) \mathrm{d}S_Q \\
&\quad = -\iint_{\bar{S}_{\mathrm{fixed}} \cup \bar{S}_{\mathrm{pm}} \cup \bar{S}_{\mathrm{fb}}} \frac{\partial^2 \phi_{S_Q}^{(1)}}{\partial t \partial n_Q^{(0)}} \left(\frac{1}{r_{PQ}} \right) \mathrm{d}S_Q \\
&+ \{\ddot{X}^{(1)}\}_{\mathrm{pm}} \cdot \left[\iint_{\bar{S}_{\mathrm{pm}}} \left(\frac{1}{r_{PQ}} \right) \{\mathbf{n}_Q^{*(0)}\} \mathrm{d}S_Q \right] \\
&+ \{\ddot{X}^{(1)}\}_{\mathrm{fb}} \cdot \left[\iint_{\bar{S}_{\mathrm{fb}}} \left(\frac{1}{r_{PQ}} \right) \{\mathbf{n}_Q^{*(0)}\} \mathrm{d}S_Q \right] \\
&- \iint_{\bar{S}_{\mathrm{fs}}} [-g\eta_S^{(1)}] \frac{\partial}{\partial n_Q^{(0)}} \left(\frac{1}{r_{PQ}} \right) \mathrm{d}S_Q
\end{aligned} \tag{20}
$$

$$\begin{aligned}
&\{\ddot{X}^{(1)}\}_{\mathrm{fb}} \cdot \left[\iint_{\bar{S}_{\mathrm{fb}}} \left(\frac{1}{r_{PQ}}\right) \{\mathbf{n}_Q^{*(0)}\} \mathrm{d}S_Q\right] = [M]^{-1} \\
&\left\{ -\rho \iint_{\bar{S}_{\mathrm{fb}}} \frac{\partial \phi_{S_Q}^{(1)}}{\partial t} \{\mathbf{n}_Q^{*(0)}\} \mathrm{d}S_Q + \right. \\
&\quad \left. -\rho \iint_{\bar{S}} \frac{\partial \phi_{I_Q}^{(1)}}{\partial t} \{\mathbf{n}_Q^{*(0)}\} \mathrm{d}S_Q - [C^{(0)}]\{\dot{X}^{(1)}\} - [K^{(0)}]\{X^{(1)}\} \right\}. \\
&\left[\iint_{\bar{S}_{\mathrm{fb}}} \left(\frac{1}{r_{PQ}}\right) \{\mathbf{n}_Q^{*(0)}\} \mathrm{d}S_Q\right] = \\
&-\rho [M]^{-1} \left(\iint_{\bar{S}_{\mathrm{fb}}} \frac{\partial \phi_{S_Q}^{(1)}}{\partial t} \{\mathbf{n}_Q^{*(0)}\} \mathrm{d}S_Q\right) \\
&\left(\iint_{\bar{S}_{\mathrm{fb}}} \left(\frac{1}{r_{PQ}}\right) \{\mathbf{n}_Q^{*(0)}\} \mathrm{d}S_Q\right) - \rho [M]^{-1} \{\mathbf{F}'\}.
\end{aligned} \tag{21}$$

3 Second-order effects

The second-order effects can be partially computed from the first-order solution by considering the interaction of two arbitrary first-order quantities. The complete second-order solution, however, involves also the effects of the second-order potential. In the present stage of the development, the contribution from the second-order potential is no computed, rendering an approximation that is sufficient for the computation of mean-drift forces and for problems for which its is known, a priori, that its effect may be neglected.

The second-order forces can be computed from the general force expression (22). According to the weakly non-linear hypothesis, the integral over the wetted surface can be split into two components: a mean-wetted surface and a periodic component that oscillates along the body's waterline, as shown in Eq. (25), which is obtained by substituting equations (23) and (24) into Eq. (22):

$$\mathbf{F} = -\rho \iint_{S_B(t)} \left(\frac{\partial \varphi_Q}{\partial t} + \frac{1}{2} \nabla \varphi_Q \cdot \nabla \varphi_Q + g z_Q \right) \mathbf{n}_Q \mathrm{d}S \tag{22}$$

$$\varphi|_z = \varphi|_{z=0} + \left.\frac{\partial \varphi}{\partial z}\right|_{z=0} z + \cdot \tag{23}$$

$$\varphi|_{S_W} = \varphi|_{\bar{S}_B} + \nabla \varphi\Big|_{\bar{S}_B} \cdot [\mathbf{x}_Q(t) - \bar{\mathbf{x}}_Q]. \tag{24}$$

Since no current effect is considered, the zeroth-order free-surface elevation can be neglected and the quantities above the mean water level can be collected up to first order. In addition, only the first terms in Taylor series are retained, because the integration of variable z over the water columns would provide terms of order 2:

$$\begin{aligned}
\mathbf{F} = &-\rho \iint_{\bar{S}_B} \left(\frac{\partial \varphi_Q}{\partial t} + \frac{1}{2} \nabla \varphi_Q \cdot \nabla \varphi_Q + g z_Q \right) \mathbf{n}_Q \mathrm{d}S \\
&+ \oint_{WL} \int_0^{(\eta_Q - z_Q)} \left(\frac{\partial \varphi_Q}{\partial t} + \frac{1}{2} \nabla \varphi_Q \cdot \nabla \varphi_Q + g z_Q \right) \mathbf{n}_Q \mathrm{d}z \mathrm{d}l.
\end{aligned} \tag{25}$$

Retaining only second-order quantities, the integration of the first term can be performed, as shown in Eq. (26), which is simplified by considering the relation $\mathbf{n}^{(1)} = \alpha^{(1)} \wedge \mathbf{n}^{(0)}$, leading Eq. (27):

$$\begin{aligned}
\iint_{\bar{S}_B} \frac{\partial \varphi_Q}{\partial t} \mathbf{n} \mathrm{d}S = &\iint_{\bar{S}_B} \left[\frac{\partial \varphi_Q^{(2)}}{\partial t} + \nabla \frac{\partial \varphi_Q^{(1)}}{\partial t} \cdot \mathbf{x}_Q^{(1)} \right] \mathbf{n}_Q^{(0)} \mathrm{d}S \\
&+ \iint_{\bar{S}_B} \frac{\partial \varphi_Q^{(1)}}{\partial t} \mathbf{n}_Q^{(1)} \mathrm{d}S + \iint_{\bar{S}_B} \frac{\partial \varphi_Q^{(0)}}{\partial t} \mathbf{n}_Q^{(2)} \mathrm{d}S
\end{aligned} \tag{26}$$

$$\begin{aligned}
&\iint_{\bar{S}_B} \frac{\partial \varphi_Q}{\partial t} \mathbf{n} \mathrm{d}S = \iint_{\bar{S}_B} \\
&\left\{ \frac{\partial \varphi_Q^{(2)}}{\partial t} + \nabla \frac{\partial \varphi_Q^{(1)}}{\partial t} \cdot [\mathbf{x}_G^{(1)} + \alpha^{(1)} \wedge (Q^{(0)} - G^{(0)})] \right\} \mathbf{n}_Q^{(0)} \mathrm{d}S \\
&\quad + \alpha^{(1)} \wedge \iint_{\bar{S}_B} \frac{\partial \varphi_Q^{(1)}}{\partial t} \mathbf{n}_Q^{(0)} \mathrm{d}S.
\end{aligned} \tag{27}$$

The integration of the velocity quadratic term can be expanded similarly in Eq. (28) keeping only second-order quantities:

$$\frac{1}{2} \iint_{\bar{S}_B} \nabla \varphi_Q \cdot \nabla \varphi_Q \mathbf{n}_Q \mathrm{d}S = \frac{1}{2} \iint_{\bar{S}_B} \nabla \varphi_Q^{(1)} \cdot \nabla \varphi_Q^{(1)} \mathbf{n}_Q^{(0)} \mathrm{d}S. \tag{28}$$

The integration of the third term over the mean-wetted surface in Eq. (25) is performed according to (29):

$$\begin{aligned}
&\iint_{\bar{S}_B} g z_Q \mathbf{n}_Q \mathrm{d}S = \iint_{\bar{S}_B} g z_Q^{(0)} \mathbf{n}_Q^{(2)} \mathrm{d}S + \iint_{\bar{S}_B} g z_Q^{(1)} \mathbf{n}_Q^{(1)} \mathrm{d}S \\
&\quad + \iint_{\bar{S}_B} g z_Q^{(2)} \mathbf{n}_Q^{(0)} \mathrm{d}S \\
&= g \alpha^{(2)} \wedge (0, 0, \forall) \\
&\quad + g \alpha^{(1)} \wedge \iint_{\bar{S}_B} z_Q^{(1)} \mathbf{n}_Q^{(0)} \mathrm{d}S + g \iint_{\bar{S}_B} z_Q^{(2)} \mathbf{n}_Q^{(0)} \mathrm{d}S.
\end{aligned} \tag{29}$$

Finally, the integration over the water column is computed from Eq. (30), which may be simplified into Eq. (31):

$$\oint_{WL}\int_0^{(\eta-zQ)}\left(\left.\frac{\partial\varphi^{(1)}}{\partial t}\right|_{z=0}+\left.\frac{\partial^2\varphi^{(1)}}{\partial z\partial t}\right|_{z=0}z\right)\left(\mathbf{n}^{(0)}+\left.\frac{\partial\mathbf{n}^{(0)}}{\partial z}\right|_{z=0}z+\mathbf{n}^{(1)}\right)\mathrm{d}z\mathrm{d}l$$
$$=\oint_{WL}\left[\left.\frac{\partial\varphi^{(1)}}{\partial t}(\eta^{(1)}-zQ^{(1)})\mathbf{n}^{(0)}\right|_{z=0}+\left.\frac{\partial\varphi^{(1)}}{\partial t}(\eta^{(0)}-zQ^{(0)})\mathbf{n}^{(1)}\right|_{z=0}\right]\mathrm{d}S \tag{30}$$

$$\frac{1}{2}\oint_{WL}\{\eta^{(1)}-[z_G^{(1)}+\alpha_x^{(1)}(y-y_G)-\alpha_y^{(1)}(x-x_G)]\}^2\mathbf{n}^{(0)}\mathrm{d}l. \tag{31}$$

Differently from an approach in frequency domain, in time-domain computations, the second-order forces already consider both the difference- and sum-frequency components that arise from the action of a regular wave. Therefore, there is no need to solve the second-order forces in different ways for the difference and sum-frequency problems. The second-order hydrodynamic forces are then summarized in Eq. (32):

$$\mathbf{F}^{(2)}=-\rho\iint_{\bar{S}_B}\left(\frac{\partial\varphi_Q^{(1)}}{\partial t}+gz_Q^{(1)}\right)\mathbf{n}_Q^{(1)}\mathrm{d}S$$
$$-\rho\iint_{\bar{S}_B}\left[\frac{1}{2}\nabla\varphi_Q^{(1)}\cdot\nabla\varphi_Q^{(1)}+\mathbf{x}_Q^{(1)}\cdot\left(\frac{\partial\nabla\varphi_Q^{(1)}}{\partial t}\right)\right]\mathbf{n}_Q^{(0)}\mathrm{d}S$$
$$+\frac{1}{2}\rho g\oint_{WL}[\eta_Q^{(1)}-(z_G^{(1)}+(y_Q-y_G^{(0)})\alpha^{(1)}$$
$$-(x_Q-x_G^{(0)})\alpha^{(2)})]^2\mathbf{n}_Q^{(0)}\mathrm{d}l. \tag{32}$$

4 Numerical method

4.1 Geometry—NURBS approach

The geometry of the problem is described in terms of Non-Uniform Rational Basis Splines (NURBS) in ".igs" format file [20, 42]. In this paper, only basic information regarding the application of the approach to the panel method will be presented. It is important to remind, first, that the boundary element method requires only surfaces to be modelled, and therefore, no references concerning solids will be made in this text.

Geometries are defined based on Eq. (33), where p is the degree of the basis spline, u are the coordinates in the parametric domain, and u_i are the knots vector in the interior region. The spline function is defined based on the recurrence equation (34) for $p > 0$, which is piecewise continuous:

$$N_{i,p}(u)=\frac{u-u_i}{u_{i+p}-u_i}N_{i,p-1}(u)$$
$$+\frac{u_{i+p+1}-u}{u_{i+p+1}-u_{i+1}}N_{i+1,p-1}(u),\ p>0 \tag{33}$$

$$N_{i,0}(u)=\begin{cases}1, & \text{if } u_i\le u<u_{i+1}\\ 0, & \text{if } u<u_i \text{ or } u\ge u_{i+1}.\end{cases} \tag{34}$$

The surface is built by the superposition of several orthogonal polynomials in the two orthogonal directions u and v, which describe the surface domain. Although the surface domain can be generic, because the u knots and v knots are arbitrary, it is convenient to "scale" it into the square of dimensions $[0, 1] \times [0, 1]$ to simplify the algebraic manipulations. The ith basis function of degree k is null in the entire domain, but in the range $[u_i, u_{i+k+1}]$, so the basis functions have a local influence region. This makes it possible to represent almost any smooth continuous arbitrary function using NURBS without demanding a very large computational effort.

The NURBS surface is defined by Eq. (35), where $\mathbf{C}_{ij}$ are the control points of the surface and w_{ij} the respective weights. The description of the entire surface is performed using the weights, control points, and knot vectors, providing a very robust format that requires a relatively small amount of memory:

$$S(u,v)=\begin{Bmatrix}x(u,v)\\ y(u,v)\\ z(u,v)\end{Bmatrix}$$
$$=\frac{\sum_{i=1}^{N_u}\sum_{j=1}^{N_v}w_{ij}\mathbf{C}_{ij}N_{i,p}(u)N_{j,p}(v)}{\sum_{i=1}^{N_u}\sum_{j=1}^{N_v}w_{ij}N_{i,p}(u)N_{j,p}(v)},0\le u\le 1,0\le v\le 1. \tag{35}$$

The parametrization functions $x(u, v)$, $y(u, v)$, and $z(u, v)$ map the surface domain into the patch region, which means that all evaluations that should be done in the physical space can be performed in the parametric domain UV. This is an important fact because, being the domain a regular unitary region, the Jacobian (Eq. (36)) can be used to change the computations from the physical space to the parametric one:

$$|J(u,v)|=\left\|\frac{\partial S}{\partial u}\wedge\frac{\partial S}{\partial v}\right\|. \tag{36}$$

4.2 Potential function and other quantities

The solution of the BVP is described using a geometry-independent B-spline approach, in which the solution is continuous inside each patch and the spline of order k is generic, providing the $k - 1$ continuous derivatives inside the patches.

In this approach, the solution can be discontinuous for the different patches, since no additional constrains are imposed in the edges of each patch. To keep the method robust in terms of geometry description, the continuity of the solution among patches is not enforced by the numerical scheme. In fact, this assumption is not unusual; it was adopted, for example, in a higher order method proposed by Maniar [39] and also in the low-order approach presented in [55]. Since no hypothesis regarding the value of the potential function in the edges of a patch is made, an additional "hidden layer" of knots is required to avoid the potential function to be null at all edges. The hidden layer is created by repeating the first and last knots k (polynomial degree).

The velocity and acceleration potentials and also the free-surface elevation are all represented in the generic form of Eq. (37), where $\phi_{i,j}^{p}$ are the coefficients corresponding to the ith basis function in direction u and jth basis function in direction of the pth patch of the domain. The basis functions have degree k_u , k_v in the u and v directions, respectively[2]:

$$\varphi(u,v)=\sum_{p=0}^{N_p}\sum_{i=0}^{N_u}\sum_{j=0}^{N_v}\phi_{i,j}^{p}N_i^{k_u,p}(u)N_j^{k_v,p}(v). \tag{37}$$

The computation of the velocity field upon the body surface is required for the evaluation of the second-order loads. In the present approach, this computation can be performed in a very straightforward manner in the parametric space by making use of the analytic derivatives of the shape functions (Eq. (38)):

$$\begin{aligned}\frac{\partial\varphi}{\partial u}(u,v)&=\sum_{p=0}^{N_p}\sum_{i=0}^{N_u}\sum_{j=0}^{N_v}\phi_{i,j}^{p}\frac{\partial N_i^{k_u,p}(u)}{\partial u}N_j^{k_v,p}(v)\\ \frac{\partial\varphi}{\partial v}(u,v)&=\sum_{p=0}^{N_p}\sum_{i=0}^{N_u}\sum_{j=0}^{N_v}\phi_{i,j}^{p}N_i^{k_u,p}(u)\frac{\partial N_j^{k_v,p}(v)}{\partial v}.\end{aligned} \tag{38}$$

The problems addressed in the present work only require the computation of first-order derivatives. The transformation between physical and parametric space is performed using the chain rule presented generically for the u direction in Eq. (39), which can be applied analogously for the v direction:

$$\begin{aligned}\left.\frac{\partial\varphi}{\partial u}\right|_{(u,v)}=&\left.\frac{\partial\varphi}{\partial x}\right|_{(x(u,v),y(u,v),z(u,v))}\left.\frac{\partial x}{\partial u}\right|_{(u,v)}+\left.\frac{\partial\varphi}{\partial y}\right|_{(x(u,v),y(u,v),z(u,v))}\left.\frac{\partial y}{\partial u}\right|_{(u,v)}+\\ &\left.\frac{\partial\varphi}{\partial z}\right|_{(x(u,v),y(u,v),z(u,v))}\left.\frac{\partial z}{\partial u}\right|_{(u,v)}.\end{aligned} \tag{39}$$

Table 1 Computation time for influence matrices evaluation for a mesh of 64 panels

Number of Gaussian points	Time elapsed (s)
2	0.13
4	0.21
6	0.35
8	0.55
10	0.80
20	3.05
40	13.99
80	85.06

The evaluation of $\partial\varphi/\partial x$, $\partial\varphi/\partial y$, and $\partial\varphi/\partial z$ is then performed using Eq. (41). Here, one should notice that an additional relation was imposed (Eq. (40)) based on the non-flux condition on the body boundary. This is done to match the number of equations and variables:

$$\left.\frac{\partial\varphi}{\partial n}\right|_{(u,v)}=\left.\left(\frac{\partial\varphi}{\partial x},\frac{\partial\varphi}{\partial y},\frac{\partial\varphi}{\partial z}\right)\right|_{(x(u,v),y(u,v),z(u,v))}\cdot\mathbf{n}(u,v) \tag{40}$$

$$\left\{\begin{matrix}\dfrac{\partial\varphi}{\partial x}\\ \dfrac{\partial\varphi}{\partial y}\\ \dfrac{\partial\varphi}{\partial z}\end{matrix}\right\}_{(x(u,v),y(u,v),z(u,v))}=\begin{bmatrix}\dfrac{\partial x}{\partial u}&\dfrac{\partial y}{\partial u}&\dfrac{\partial z}{\partial u}\\ \dfrac{\partial x}{\partial v}&\dfrac{\partial y}{\partial v}&\dfrac{\partial z}{\partial v}\\ n_x&n_y&n_z\end{bmatrix}_{(u,v)}^{-1}\left\{\begin{matrix}\dfrac{\partial\varphi}{\partial u}\\ \dfrac{\partial\varphi}{\partial v}\\ \dfrac{\partial\varphi}{\partial n}\end{matrix}\right\}_{(u,v)}. \tag{41}$$

In the low-order approach, there are specific equations for the integration of the self-influence components in the computation of the influence matrix for the source and dipole terms. However, in the higher order approach, there is a significant contribution of curvature effects in these components for both source and dipole terms, and this point will be discussed next.

4.3 Integration of the source and dipole terms

The Green's identity assumed in the solution of the BVP was given in Eq. (19), and in our case, the solid angle is always 2π, since no collocation points are located in the edges. The integrands will always have two main

---

[2] In the present work the same degree was always used in both directions.

functions, the sources and dipoles, both containing singularities when the field and source points are coincident. The integrands can be discretized using the B-spline approximation, providing Eqs. (42) and (43):

$$\begin{aligned}&\int_0^1\int_0^1 \varphi(u,v)\frac{\partial}{\partial n(u,v)}\left(\frac{1}{r_{PQ}(u,v)}\right)|J(u,v)|\mathrm{d}v\mathrm{d}u\\ &\quad=\sum_{p=0}^{N_p}\sum_{i=0}^{N_u}\sum_{j=0}^{N_v}\phi^p_{i,j}\int_{u_i}^{u_{i+k_u+1}}\int_{v_j}^{v_{j+k_v+1}}\\ &N_i^{k_u,p}(u)N_j^{k_v,p}(v)\frac{\partial}{\partial n(u,v)}\left(\frac{1}{r_{PQ}(u,v)}\right)|J(u,v)|\mathrm{d}v\mathrm{d}u\end{aligned}\tag{42}$$

$$\begin{aligned}&\int_0^1\int_0^1 \frac{\partial\varphi}{\partial n}(u,v)\left(\frac{1}{r_{PQ}(u,v)}\right)|J(u,v)|\mathrm{d}v\mathrm{d}u\\ &\quad=\sum_{p=0}^{N_p}\sum_{i=0}^{N_u}\sum_{j=0}^{N_v}\frac{\partial\phi^p_{i,j}}{\partial n}\int_{u_i}^{u_{i+k_u+1}}\int_{v_j}^{v_{j+k_v+1}}\\ &N_i^{k_u,p}(u)N_j^{k_v,p}(v)\left(\frac{1}{r_{PQ}(u,v)}\right)|J(u,v)|\mathrm{d}v\mathrm{d}u.\end{aligned}\tag{43}$$

To improve the numerical integration procedure, there are different considerations to be done about the integration process depending on the position of the collocation point. To illustrate the difficulties associated with the integration process, the case of a sphere in uniform flow is used for the evaluation of the influence matrix. The integrand (42) is particularly difficult to be evaluated in the near field and self-influence due to the abrupt variations in the values of the functions near the singular point. The computations are performed using Gauss–Legendre quadrature, as shown in Eq. (44), where Ng_u and Ng_v are the number of Gaussian

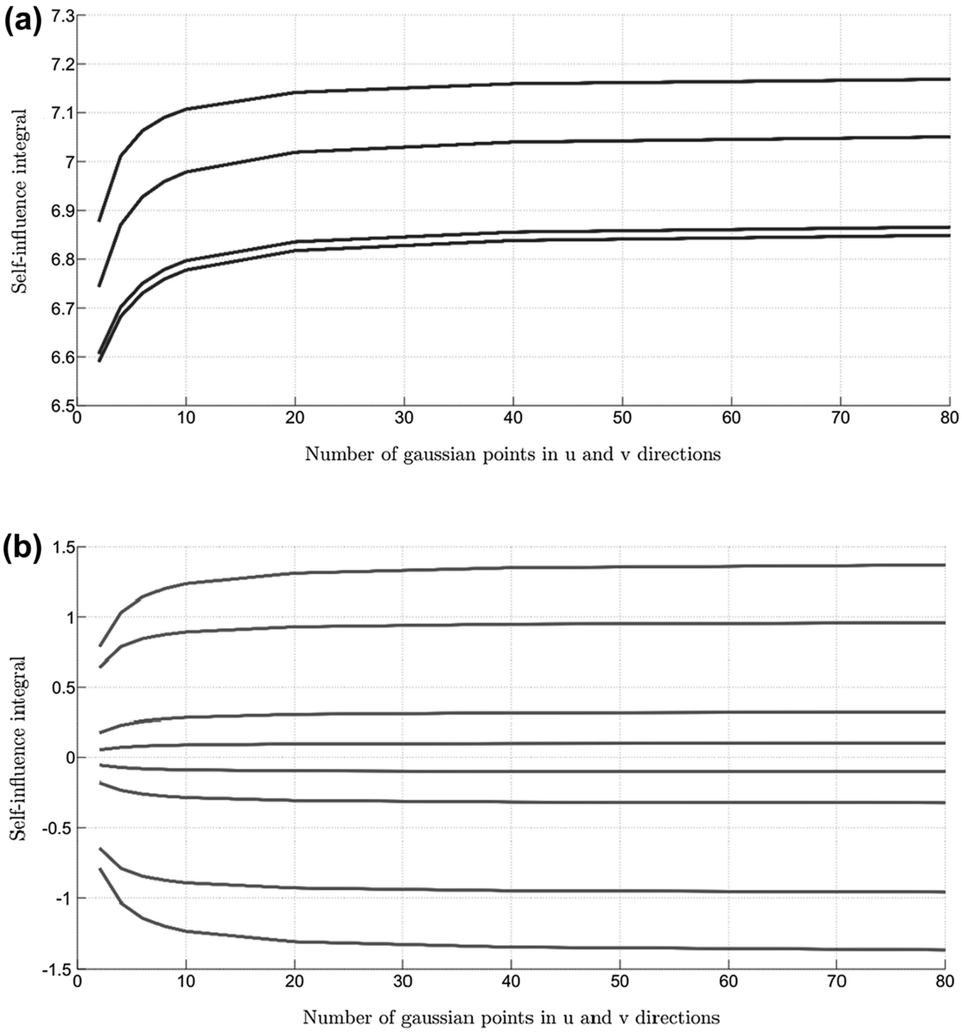

Fig. 2 Convergence analysis of the matrices A and B an the self-influence integral changing the number of Gaussian points

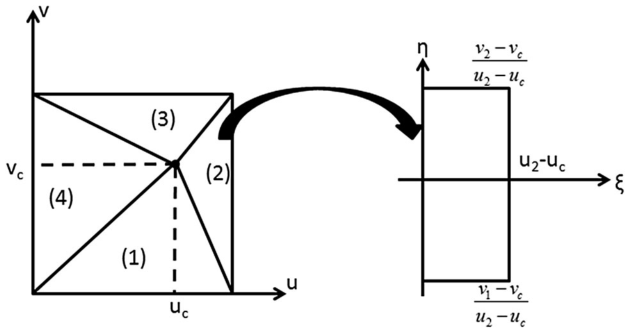

Fig. 3 Domain splitting into four triangles and integration domain considering the region (2) using bi-quadratic transformation

points in u and v directions, w_m and w_n are the weights, and u_m, v_n are the Gaussian points:

$$\int_{u_i}^{u_{i+k_u+1}} \int_{v_j}^{v_{j+k_v+1}} f(u,v)\mathrm{d}v\mathrm{d}u \approx \sum_{m=1}^{Ng_u} \sum_{n=1}^{Ng_v} w_m w_n f(u_m, v_n). \tag{44}$$

The influence matrix is composed of the dipole and source elements, denoted by A and B matrices, respectively. To simplify the analysis, the zero-order polynomial distribution is assumed, and therefore, the values inside each are constant. The study was performed assuming 2, 4, 6, 8, 10, 20, 40, and 80 Gaussian points in each direction. The sphere was divided considering panels with areas of less than 0.2 m^2 for a sphere of unitary radius, generating a total number of 64 panels.

The variation in computational time when changing the number of Gaussian points can be seen in Table 1 (computed in Matlab® environment). A convergence analysis considering the self-influence terms in matrices A and B can be seen in Fig. 2. It makes evident that there is a low rate of convergence when using a Gauss–Legendre approach, since, even for a large number of points (more than 40), the tolerance of 10^{-4} could not be achieved.

To improve the integration process, an analytic desingularization method was adopted, considering the bi-quadratic transformation method, as introduced by Maniar [39]. However, the method originally proposed was applied to a B-spline geometry representation; therefore, an extension of the method was required to take NURBS geometries into account. Moreover, the approach described by Maniar [39] requires the approximation of the integrand by an expansion series and an analytic integration of each individual component, considering both the source/dipole terms and the transformation Jacobian, rendering the numerical procedure rather complex.

In the present work, the procedure proposed by Kim et al. [25] was applied, using the bi-quadratic transformation for the analytic desingularization and then Gauss–Legendre quadrature in the "new" non-singular integrand considering the NURBS geometry description. The domain is decomposed into four different zones (triangles), keeping the singular point only at the common vertex. The procedure is illustrated in Fig. 3, where u_c and v_c are the parametric coordinates of the collocation points and the right side picture is the integration domain after applying the bi-quadratic transformation, as described in Eq. (45) concerning region 2. The transformations of the other regions are obtained analogously, as shown in Eqs. (47), (48), and (46) for regions 1, 3, and 4, respectively.

$$\begin{aligned} u - u_c &= \xi \\ v - v_c &= \xi\eta \end{aligned} \tag{45}$$

$$\begin{aligned} u - u_c &= -\xi \\ v - v_c &= -\xi\eta \end{aligned} \tag{46}$$

$$\begin{aligned} u - u_c &= \xi\eta \\ v - v_c &= \xi \end{aligned} \tag{47}$$

$$\begin{aligned} u - u_c &= -\xi\eta \\ v - v_c &= -\xi \end{aligned} \tag{48}$$

The self-influence terms can be written as in Eqs. (49) and (51), where the terms I_{Dk} and I_{Sk} are the integrals over each individual triangle [region 2 is assumed in the example in Eqs. (50) and (52)] and summing up the contributions over the four different regions. These last equations are not singular and can be evaluated numerically using Gauss–Legendre quadrature directly:

$$\int_{u_1}^{u_2} \int_{v_1}^{v_2} N_i(u)N_j(v) \frac{\partial}{\partial n(u,v)} \left(\frac{1}{r_{PQ}(u,v)} \right) |J(u,v)| \mathrm{d}v\mathrm{d}u = \sum_{k=1}^{4} I_{Dk} \tag{49}$$

$$I_{D2} = \int_0^{u_2 - u_c} \int_{\frac{v_1 - v_c}{u_2 - u_c}}^{\frac{v_2 - v_c}{u_2 - u_c}} N_i(\xi + u_c) N_j(\xi\eta + v_c) \frac{\mathbf{r}_{PQ}(\xi + u_c, \xi\eta + v_c) \cdot \mathbf{N}(\xi + u_c, \xi\eta + v_c)}{r_{PQ}^3(\xi + u_c, \xi\eta + v_c)} \left| \frac{\partial \mathbf{r}_{PQ}}{\partial \xi} \wedge \frac{\partial \mathbf{r}_{PQ}}{\partial \eta} \right| \mathrm{d}\eta\mathrm{d}\xi \tag{50}$$

$$\int_{u_1}^{u_2} \int_{v_1}^{v_2} N_i(u)N_j(v) \left(\frac{1}{r_{PQ}(u,v)} \right) |J(u,v)| \mathrm{d}v\mathrm{d}u = \sum_{k=1}^{4} I_{Sk} \tag{51}$$

$$I_{S2} = \int_0^{u_2-u_c} \int_{\frac{v_1-v_c}{u_2-u_c}}^{\frac{v_2-v_c}{u_2-u_c}} N_i(\xi+u_c)N_j(\xi\eta+v_c) \tag{52}$$
$$\frac{1}{r_{PQ}(\xi+u_c,\xi\eta+v_c)}\left|\frac{\partial \mathbf{r}_{PQ}}{\partial \xi}\wedge\frac{\partial \mathbf{r}_{PQ}}{\partial \eta}\right| \mathrm{d}\eta \mathrm{d}\xi.$$

The numerical integration using 4 Gaussian points per region (16 in total concerning the entire panel) for the same sphere studied earlier provided an accuracy of less than 10^{-6}, which could not be achieved by direct integration even when using 80 Gaussian points for the singular integrand. The integration of the other terms near the main diagonal of the linear system (but not the self-influence) can be performed using an adaptive method until the desired accuracy is achieved. This procedure usually requires less than nine points for a 10^{-6} threshold, assuming a monotonic convergence.

4.4 The importance of the collocation points and linear system setup

The setup of the linear system is not a trivial task in the higher order method compared to the low-order approach. Indeed, due to the additional (hidden) layers concerning the patch boundaries, there are more variables (spline coefficients) than equations if we consider only a single collocation point per panel (an approach that is usual in the low-order method). There are several ways to overcome this limitation and three different methodologies were tested: two of them choosing the same number of collocation points and B-spline unknown coefficients, thus obtaining a determined linear system, and a third approach assuming more than a single collocation point per panel, thus leading to an overdetermined linear system. In the first case, the linear system can be solved directly, while for the latter, the least square approach proposed by Kim et al. [25] is applied.[3] The B-spline degree adopted in the analysis is fixed in 2 for all the comparisons to simplify the analysis.

The first method that was evaluated is the so-called "extended" panel approach, where the panels are not taken as the interval between successive knots, but as the interval, where a shape function (spline) extends without null values (u_i, u_{i+p+1}). The collocation points are chosen as the midpoint of the not null interval as in Eq. (53), providing one collocation point per shape function. The second approach considered involves the distribution of collocation points using Legendre polynomial roots in the parametric space, while the third one places multiple collocation points inside each panel (interval of not coincident knots) to obtain an overdetermined linear system. The number of collocation points inside each panel is completely arbitrary, and in this work, four points were assumed:

$$(u_{ci}, v_{ci}) = \left(\frac{u_i + u_{i+p+1}}{2}, \frac{v_i + v_{i+p+1}}{2}\right). \tag{53}$$

When comparing the different procedures, it was found that the second method leads to a concentration of points near the patch edges if compared to the first approach. The third procedure, on the other hand, provides a more uniform distribution of collocation points. In this method, the system is defined based on Eq. (54), where m and n are the number of lines and columns, respectively, $(m \geq n)$. The solution is computed as in Eq. (55):

$$[A]_{m,n}\{c\}_{n,1} = \{B\}_{m,1} \tag{54}$$

$$\begin{aligned}([A]^T_{n,m}[A]_{m,n})\{c\}_{n,1} &= [A]^T_{n,m}\{B\}_{m,1}\\ \Rightarrow \{c\}_{n,1} &= ([A]^T_{n,m}[A]_{m,n})^{-1}[A]^T_{n,m}\{B\}_{m,1}.\end{aligned} \tag{55}$$

The performance of the alternative procedures is compared for the case of a submerged sphere of radius R in uniform flow, with the analytic solution, as shown in Eq. (56). The velocity potential distribution was evaluated in a grid of 60×60 in the parametric space, considering an uniform distribution; thus, the potential is not evaluated in the collocation points itself, unless by coincidence:

$$\begin{aligned}\phi^{(0)} &= \frac{1}{2}\frac{xR^3}{(x^2+y^2+z^2)^{3/2}}\\ \Rightarrow \varphi^{(0)} &= Ux + \frac{1}{2}\frac{xR^3}{(x^2+y^2+z^2)^{3/2}}.\end{aligned} \tag{56}$$

The comparison of the potential values computed with the different techniques and the analytic solution, for a 64 panel mesh, is presented in Fig. 4. It can be seen that only the procedure that considers multiple collocation points per panel has converged in the entire domain. The method using the Legendre roots showed good agreement at the edges of the sphere but not in the central region, and this is probably due to the lower number of collocation points in

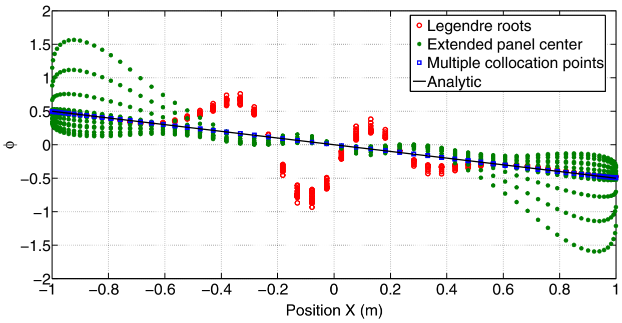

Fig. 4 Comparison among several collocation points choice considering the disturbance potential due to an incident unitary flow

---

[3] This could also be performed using a Galerkin approach Maniar [39].

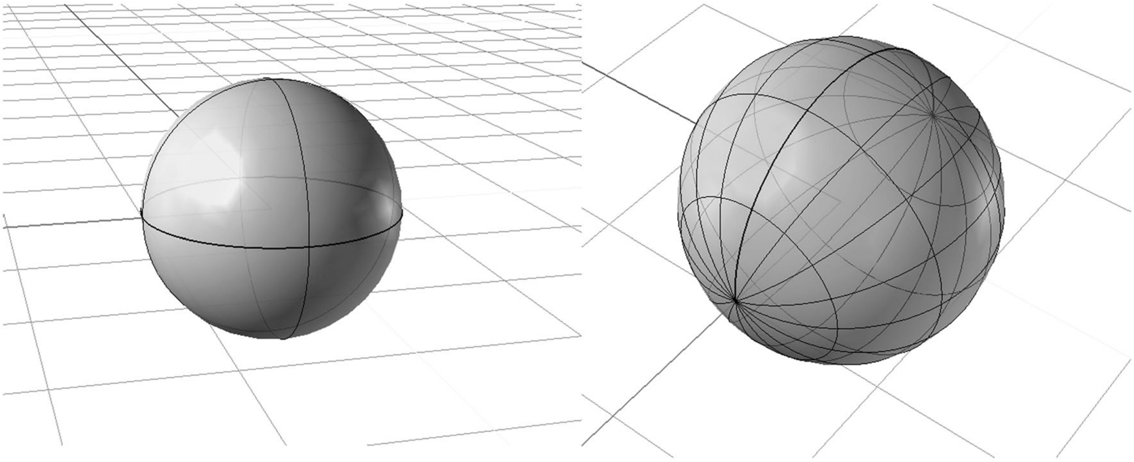

Fig. 5 Comparison of mesh topology concerning a sphere described by a single patch (right) and by two patches (left)

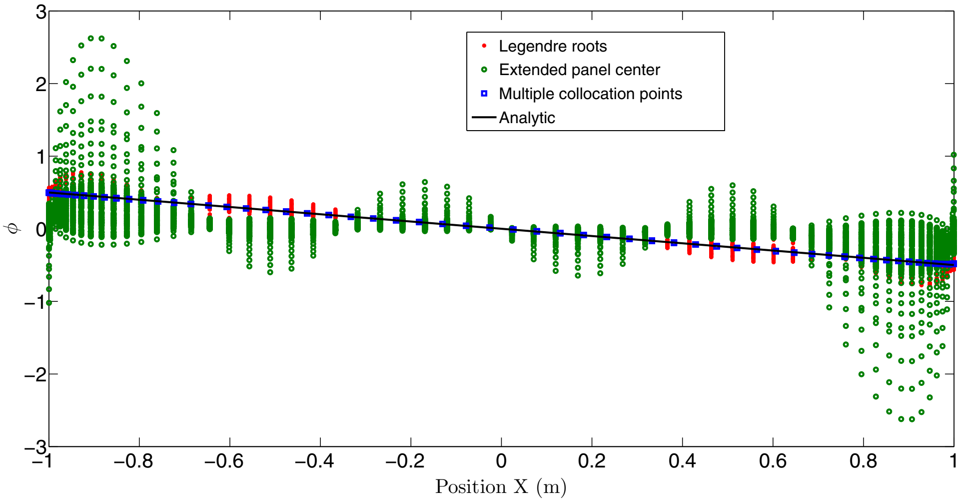

Fig. 6 Comparison among several collocation points choice considering the disturbance potential due to an incident unitary flow, considering a sphere described by two patches

the central region when following this specific approach. The extended panel method provides a good agreement near the center of the sphere but not at the edges and there are large "fluctuations" in the values along the azimuth angle (for a constant x value) mainly in the edges region. Something that is not expected since the flow is symmetric about the incident flow axis (x-axis). These fluctuations are much reduced in the Legendre root approach and negligible in the case of multiple collocation points. For this region, the latter was selected for present developments.

It should also be noticed that, due to the lack of continuity of the velocity potential across the patches, the solution may change significantly depending on the user expertise regarding mesh generation. In general, it is always better to keep larger patches instead of splitting it in several small ones due to the continuity of the solution inside each individual patch, defined by construction.

To investigate this behavior, the same sphere that was described considering a single patch in the previous analyses was split into two patches, as shown in Fig. 5, where the differences in mesh topology can be observed.

A similar comparison regarding the computation of the velocity potential function is shown in Fig. 6. One may realize that, although there are significant differences in the results, the approach with the multiple collocation points per panel is once again less sensitive, with a general good agreement with the analytic solution. Again, this speaks in its favour as the preferable choice for building the linear system.

4.5 Comparisons concerning the spline degree

To verify the influence of the spline degree on the distribution of the potential functions, the method of multiple collocation points per panel was used while varying the spline degree from 0 (constant inside each panel) to 3 (cubic).

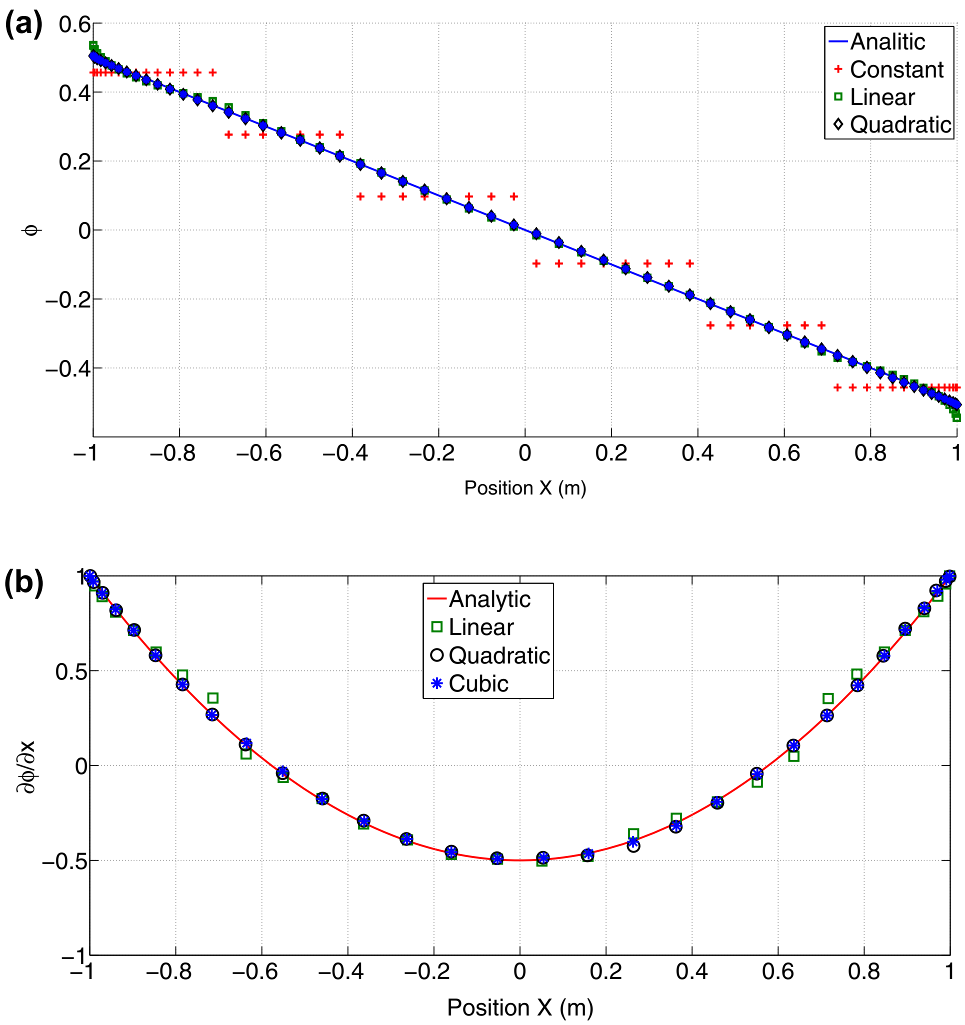

Fig. 7 Comparison among several degrees of spline approximation and analytic solution concerning the disturbance potential (**a**) and velocity in x direction (**b**) around a sphere under incident flow

The results regarding the distribution of the disturbance potential can be seen in Fig. 7. As expected when dealing with a spheric body geometry, it can be seen that there is a gain in accuracy when changing from a low order (zero order) to a higher order approach and that, in the latter case, only small improvements arise when changing from a linear to a quadratic or cubic model. The comparison of the disturbance velocity is shown in Fig. 7, where good agreement is verified overall, but for the linear distribution near the ± 0.8 m position.

5 The wave–body interaction problem

In this section, some relevant aspects regarding the numerical solution of the boundary integral equations (19) and (20) will be addressed. First, it should be noticed that since we perform the computations on the mean surfaces and not on the exact (instantaneous) surfaces, the sources, dipoles, normal vectors, and integration domains remain constant in time, meaning that many terms only need to be computed once.

The term concerning integration of the incident field, however, would require a new computation per time step, since the time dependent term is inside a transcendental function (see Eq. (57), in which this term is represented in its discrete version). Obviously, this is not efficient from a numerical point of view. Nonetheless, the problem can be avoided quite simply by expanding the cosine and sine terms making use of the trigonometric relations, as shown in Eqs. (58) and (59). With this procedure, the time variant term can be removed from the integral, rendering the computations more efficient. Although there is now four terms to be integrated instead of a single one, these quantities are computed only once, not requiring any additional computation during the evolution of the solution in time:

$$\begin{aligned}&\iint_{\bar{S}_{\mathrm{fixed}}\cup\bar{S}_{\mathrm{pm}}\cup\bar{S}_{\mathrm{fb}}}\frac{\partial\phi_{I_Q}^{(1)}}{\partial n_Q^{(0)}}\left(\frac{1}{r_{PQ}}\right)\mathrm{d}S_Q\\&=\sum_{p=0}^{N_p}\sum_{i=0}^{N_u}\sum_{j=0}^{N_v}\sum_{w=0}^{N_w}A_w\omega_w\int_0^1\int_0^1 e^{k_w z(u,v)}\{[-\cos\beta_w n_x(u,v)\\&\quad-\sin\beta_w n_y(u,v)]\sin(k_w x(u,v)\cos\beta_w+k_w y(u,v)\sin\beta_w\\&\quad-\omega_w t+\delta_w)+n_z(u,v)\cos(k_w x(u,v)\cos\beta_w\\&\quad+k_w y(u,v)\sin\beta_w-\omega_w t+\delta_w)\}|J(u,v)|\mathrm{d}v\mathrm{d}u\end{aligned} \tag{57}$$

$$\begin{aligned}&\sin(k_w x(u,v)\cos\beta_w+k_w y(u,v)\sin\beta_w-\omega_w t+\delta_w)\\&\quad=\sin(k_w x(u,v)\cos\beta_w+k_w y(u,v)\sin\beta_w+\delta_w)\cos(\omega_w t)\\&\quad-\sin(\omega_w t)\cos(k_w x(u,v)\cos\beta_w+k_w y(u,v)\sin\beta_w+\delta_w)\end{aligned} \tag{58}$$

$$\begin{aligned}&\cos(k_w x(u,v)\cos\beta_w+k_w y(u,v)\sin\beta_w-\omega_w t+\delta_w)\\&\quad=\cos(k_w x(u,v)\cos\beta_w+k_w y(u,v)\sin\beta_w+\delta_w)\cos(\omega_w t)\\&\quad-\sin(\omega_w t)\sin(k_w x(u,v)\sin\beta_w+k_w y(u,v)\sin\beta_w+\delta_w).\end{aligned} \tag{59}$$

5.1 Free-surface condition and the use of a numerical beach (sponge layer)

The free-surface condition is applied in the collocation points located on the mean free-surface panels and the variables are the time derivative of the free-surface elevation and potential functions at the free surface ($\partial\eta_{S_{ij}}^{(1)}/\partial t$ and $\partial\phi_{S_{ij}}^{(1)}/\partial t$), also leading to an overdetermined linear system.

The expansion of the free-surface elevation with a generic number of collocation points can be seen in Eq. (60). The linearized kinematic free-surface condition is written in the matrix form in Eq. (61), where the vectors A_1, B_1, A_2, and B_2 are the spatial derivatives of the incident wave elevation function discussed earlier:

$$\begin{aligned}&\sum_{i=1}^{N_u}\sum_{j=1}^{N_v}\frac{\partial\eta_{S_{ij}}^{(1)}}{\partial t}N_i(u_{Pk})N_j(v_{Pk})\\&=\begin{bmatrix}N_1(u_{P1})N_1(v_{P1}) & \ldots & N_{N_u}(u_{P1})N_{N_v}(v_{P1})\\ N_1(u_{P2})N_1(v_{P2}) & \ldots & N_{N_u}(u_{P2})N_{N_v}(v_{P2})\\ \vdots & \vdots & \vdots\\ N_1(u_{P4N_P})N_1(v_{P4N_P}) & \ldots & N_{N_u}(u_{P4N_P})N_{N_v}(v_{P4N_P})\end{bmatrix}\\&\begin{pmatrix}\frac{\partial\eta_{S_{11}}^{(1)}}{\partial t}\\ \frac{\partial\eta_{S_{12}}^{(1)}}{\partial t}\\ \vdots\\ \frac{\partial\eta_{S_{N_uN_v}}^{(1)}}{\partial t}\end{pmatrix}=\Big[N_{ij}(u_P,v_P)\Big]_{4.N_PXN_u.N_v}\cdot\left\{\frac{\partial\eta_{S_{ij}}^{(1)}}{\partial t}\right\}_{N_u.N_vX1}\\&=[N]\{\eta_t^{(1)}\}\end{aligned} \tag{60}$$

$$\begin{aligned}[N]\{\eta_t^{(1)}\}=&[N]\{\phi_{Sz}^{(1)}\}+\{A_1\}\cos(\omega t)+\{B_1\}\sin(\omega t))-\\&+\{A_2\}\cos(\omega t)+\{B_2\}\sin(\omega t))\\&-\{v\}\{\phi^{(1)}\}=0.\end{aligned} \tag{61}$$

The kinematic first-order condition can be solved in a procedure that is analogous to the one adopted for the integral equations according to Eq. (62). This is very convenient from a numerical point of view, because all matrices can be pre-computed, and therefore, only the vector containing the first-order quantities is updated at each time step. The solution of the dynamic free-surface condition is computed using the same approach:

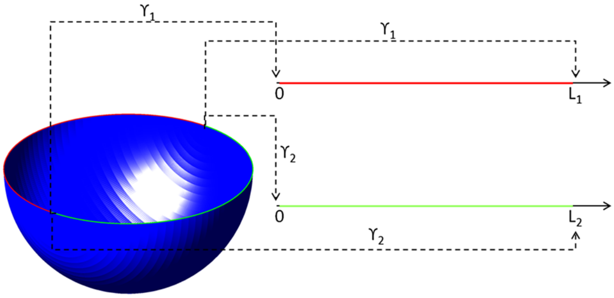

Fig. 8 Mapping from the parametric to the physical space concerning the waterline

$$
\begin{aligned}
\{\eta_t^{(1)}\} = {} & ([N]^T[N])^{-1}([N]^T[N])\{\phi_{Sz}^{(1)}\} \\
& - ([N]^T[N])^{-1}[N]^T(\{A_1\}+\{A_2\})\cos(\omega t) \\
& - ([N]^T[N])^{-1}[N]^T(\{B_1\}+\{B_2\})\sin(\omega t) \\
& - ([N]^T[N])^{-1}[N]^T\{v\}\{\phi^{(1)}\} = 0.
\end{aligned} \tag{62}
$$

5.2 Dealing with the gradient of the velocity potential time derivative

The computation of the second-order forces (Eqs. (28) to (32)) are performed considering terms on the body mean-wetted surface and body waterline. The only term that has not been defined yet is the gradient of the time derivative of the potential function. This gradient can be obtained based on Eq. (63), where the transformation matrix requires only the spline description concerning body geometry. The quantities $\dfrac{\partial^2 \phi_S}{\partial u \partial t}$ and $\dfrac{\partial^2 \phi_S}{\partial v \partial t}$ are computed directly from the solution of the first-order problem, whereas $\dfrac{\partial^2 \phi_S}{\partial n \partial t}$ comes from the body boundary condition in the acceleration potential (Eq. (15)):

$$
\left\{ \begin{array}{c} \dfrac{\partial^2 \phi_S}{\partial x \partial t} \\ \dfrac{\partial^2 \phi_S}{\partial y \partial t} \\ \dfrac{\partial^2 \phi_S}{\partial z \partial t} \end{array} \right\}_{(x(u,v),y(u,v),z(u,v))} = \begin{bmatrix} \dfrac{\partial x}{\partial u} & \dfrac{\partial y}{\partial u} & \dfrac{\partial z}{\partial u} \\ \dfrac{\partial x}{\partial v} & \dfrac{\partial y}{\partial v} & \dfrac{\partial z}{\partial v} \\ n_x & n_y & n_z \end{bmatrix}^{-1}_{(u,v)} \left\{ \begin{array}{c} \dfrac{\partial^2 \phi_S}{\partial u \partial t} \\ \dfrac{\partial^2 \phi_S}{\partial v \partial t} \\ \dfrac{\partial^2 \phi_S}{\partial n \partial t} \end{array} \right\}_{(u,v)}. \tag{63}
$$

However, for the computation of the second-order forces, a numerical problem remains concerning the definition of the waterline intersection for a generic body surface. The method that was applied for this definition is presented next.

5.3 Definition of the waterline intersection

The computation of the drift forces requires an integral on the body waterline and thus involves the solution of a difficult mathematical problem, namely, the definition of a surface–surface intersection (similar to the so-called trim problem). This task is particularly difficult when a mathematical surface is defined by means of several patches.

Many algorithms are presented in the literature for dealing with this problem, most of them requiring an iterative method or the solution of a system of partial differential equations (see, for instance, Teixeira and Creus [52], Tang and Medioni [48], Hass et al. [19]). Regarding the present numerical method, the intersection problem occurs for two different situations: the first when only the mean-wetted surface is provided, and then, there is no surface above the undisturbed waterline; the second when the full body geometry is provided, and therefore, the surface bellow the instantaneous waterline must be defined.

In general, the integration of the body waterline (WL) is performed in the several curves defined by the intersection of the body and the undisturbed free-surface elevation (WL$_i$), as illustrated in Fig. 8. The contribution of the several waterline curves is summed up using Eq. (64):

$$
\oint_{WL} F(l)\mathrm{d}l = \sum_{i=1}^{N} \oint_{WL_i} F(l)\mathrm{d}l_i. \tag{64}
$$

It is performed assuming a parametric curve $\gamma_i(s) = (x_i(s), y_i(s), z_i(s))$ that maps the physical curve in the parametric space from 0 to L_i, where $F_i(s)$ is a generic curve, as shown in Eq. (65).

$$
\oint_{WL_i} F(l)\mathrm{d}l_i = \int_0^{L_i} F_i(s)||\gamma_i'(s)||\mathrm{d}s. \tag{65}
$$

The vector $\gamma_i'(s)$ is tangent to the intersection of both surfaces, and since the undisturbed free surface is defined as $z = 0$, the vector is defined as the cross product of both normal vectors, as shown in Eq. (66):

$$
\begin{aligned}
\gamma_i'(s) &= \left(\frac{\partial S}{\partial x}, \frac{\partial S}{\partial y}, \frac{\partial S}{\partial z} \right)\Bigg|_{(x(u(s),v(s)),y(u(s),v(s)),0)} \wedge (0,0,1) \\
&= \left(\frac{\partial S}{\partial y}, -\frac{\partial S}{\partial x}, 0 \right)\Bigg|_{(x(u(s),v(s)),y(u(s),v(s)),0)}.
\end{aligned} \tag{66}
$$

A simple technique to define the surface intersection is to select an initial point in the intersection and then solve the system of coupled ordinary differential equations (67), which is performed using a Runge–Kutta–Fehlberg technique with an adaptive step size. The initial is found by application of Newton–Raphson method in the NURBS space concerning the body patches, as shown in Eq. (68).

Since the initial point computed is not always located in the corner of a patch, the ordinary differential equation is solved considering both tangent vector orientations:

$$
\begin{cases}
\dfrac{\mathrm{d}x}{\mathrm{d}s} = \dfrac{\partial S}{\partial y}\Bigg|_{(x(u(s),v(s)),y(u(s),v(s)),0)} \\
\dfrac{\mathrm{d}y}{\mathrm{d}s} = -\dfrac{\partial S}{\partial x}\Bigg|_{(x(u(s),v(s)),y(u(s),v(s)),0)}
\end{cases} \tag{67}
$$

Fig. 9 Projection of the points in the body surface intersection to the free surface

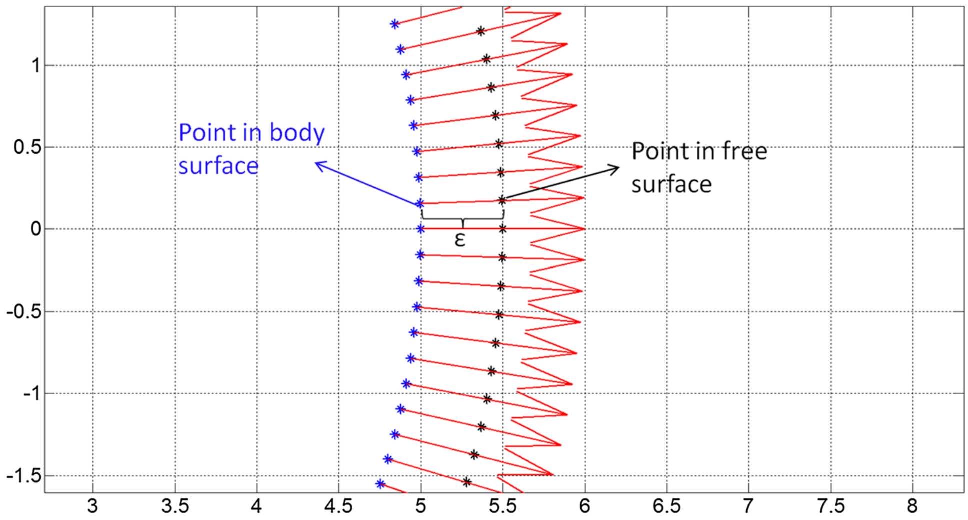

$$z(u(s=0),v(s=0))=0 \Rightarrow x(u(s=0),v(s=0)),y(u(s=0),v(s=0)). \quad (68)$$

The solution of this mathematical problem provides a set of point lists p(j), each one regarding the waterline intersection; therefore, the integral can be approximated by Eq. (69) using a trapezoidal rule for non-equally spaced data. Here, α_i denotes the weights, being 1 to the first and last points and 2 for the remaining ones:

$$\int_0^{L_i} F_i(s)||\gamma_i'(s)||\mathrm{d}s \approx \sum_{j=0}^{N_c} \sum_{i=0}^{N_{p(j)}-1} \alpha_i F_j(s_i)\sqrt{[x_j(s_{i+1})-x_j(s_i)]^2+[y_j(s_{i+1})-y_j(s_i)]^2}. \quad (69)$$

The contribution of body motions in the relative elevation of the waterline can be computed using the points obtained in the parametric space. However, the free-surface elevation requires an additional step, since the elevation is computed in terms of the parametric coordinates (u, v) of the floating body patches, which are not the same of the free-surface patches. The coordinates of the parametric space are defined by solving the system in Eq. (70) for the free-surface patches:

$$\begin{cases} x(u,v)=x_j(s_i) \\ y(u,v)=y_j(s_i) \end{cases}, i=1,2,\ldots N_p(j), \quad j=0,\ldots N_c. \quad (70)$$

From the numerical point of view, the solution of the previous problem can be difficult due to the tolerance concerning the match of body and free-surface patches. The points in the body patches are "projected" in the free-surface assuming a small tolerance ε using Eq. (71). Here, $\mathbf{n}^*$ is the unitary normal vector in the body waterline intersection pointing outward, as shown in Fig. 9, neglecting the z-component for non "wall-sided" bodies:

$$(x(u,v),y(u,v),0)_{\mathrm{fs}}=(x_j(s_i),y_j(s_i),0)_{\mathrm{body}} + \varepsilon\mathbf{n}^*|_{(x_j(s_i),y_j(s_i),0)}. \quad (71)$$

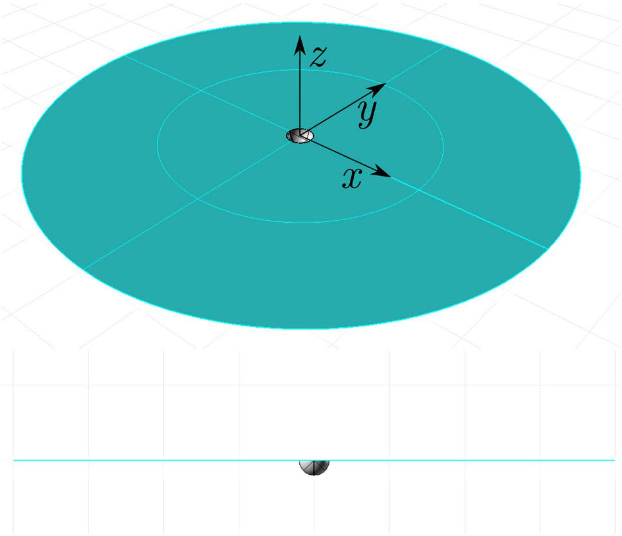

Fig. 10 Sphere and free-surface geometries

Table 2 U and V number of subdivisions in the parametric space for the sphere

Discretization	Body patch 1	Body patch 2	Free surface
Fine	6 × 6	6 × 6	30 × 30
Medium	4 × 4	4 × 4	24 × 24
Coarse	2 × 2	2 × 2	16 × 16

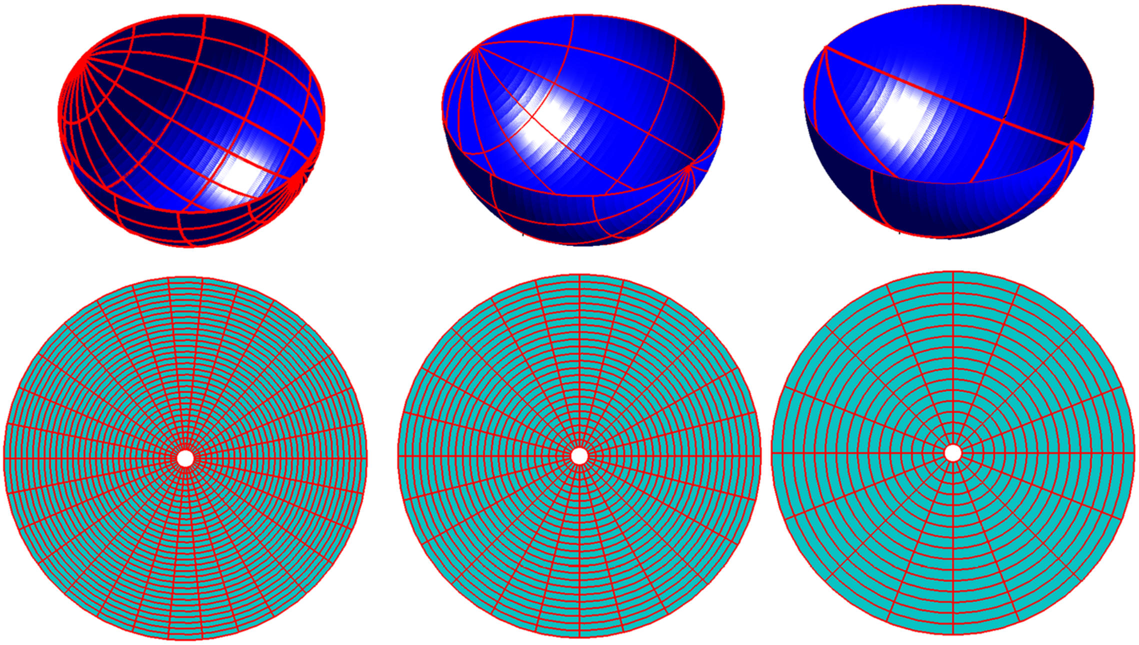

Fig. 11 Meshes adopted in the computation of the sphere: fine (left), medium (center), and coarse (right)

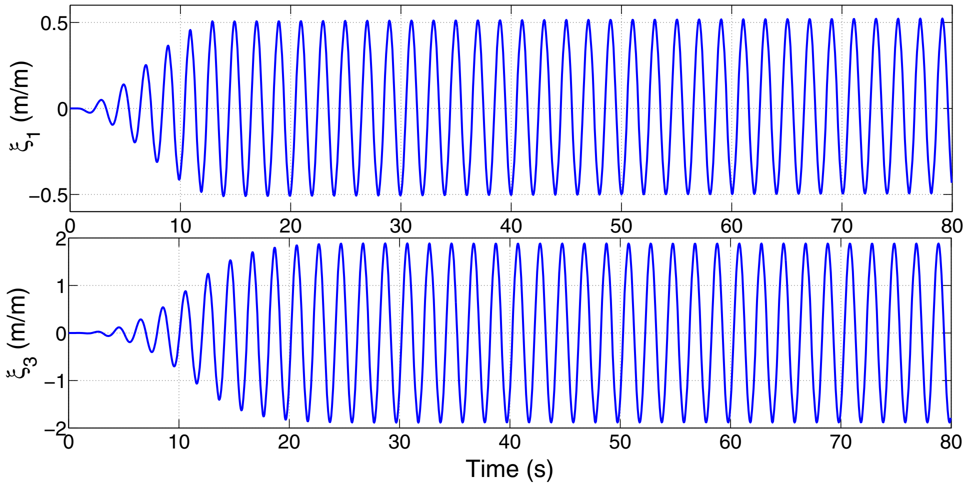

Fig. 12 Example of motion time series for a floating sphere

5.4 Time integration

The integration in time of the ordinary differential equations is performed using a standard fourth-order Runge–Kutta method. At each step of the RK4, the following calculations are performed:

1. Impose the free-surface potential, body velocities, and prescribed velocities in S_{fs}, S_{fb}, and S_{pm}, as forcing term in integral equation regarding the velocity potential to compute control points of the potential (φ_S) in S_{fb}, S_{fixed}, S_{pm} and the control points of $\frac{\partial \varphi_S}{\partial n}$ in S_{fs}.
2. Impose the time derivative of the free-surface potential and prescribed accelerations in S_{fs} and S_{pm}, as forcing term in integral equation regarding the acceleration potential to compute the control points of the time derivative of the potential ($\frac{\partial \varphi_S}{\partial t}$) in S_{fb}, S_{fixed} , S_{pm} and control points of $\frac{\partial^2 \varphi_S}{\partial t \partial n}$ in S_{fs}.
3. Compute the control points of $\frac{\partial \eta_S}{\partial t}$ from the kinematic free-surface condition using $\frac{\partial \varphi_S}{\partial n}$ computed in the velocity BVP.
4. Compute the control points of $\frac{\partial \varphi_S}{\partial t}$ from the dynamic free-surface condition using the control points of η_S.
5. Compute the body forces and moments using $\frac{\partial \varphi_S}{\partial t}$ using the control points calculated from the acceleration BVP.

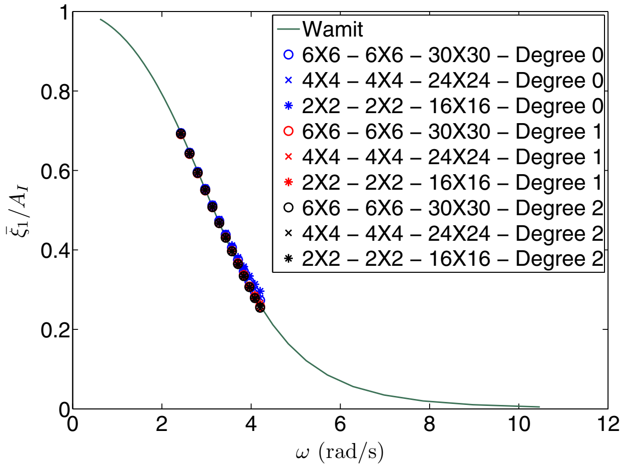

Fig. 13 Surge response operator for the hemisphere

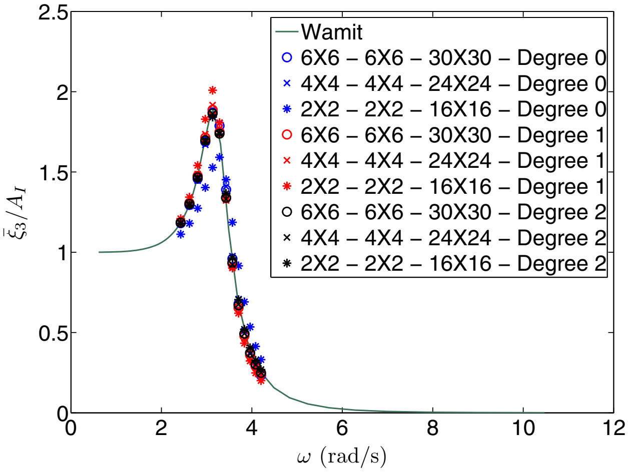

Fig. 14 Heave response operator for the hemisphere

6. Update the body velocity and position using RK4 scheme.
7. Update the free-surface potential (φ_S) and elevation (η_S) control points using RK4 scheme.

6 Numerical results

The numerical results are validated by comparing steady-state results obtained with the Higher Order Time-Domain Rabkine Panel Method (HOTDRPM) code with those obtained in frequency domain with WAMIT, both for first- and second-order quantities. For the latter, to provide a fair comparison, the second-order forces are computed considering the same geometry topology (number of patches) and NURBS degree in both methods.

As the case study for a primary validation, a floating hemisphere was considered due to its simple geometry. Since the second-order loads requires the computation of local quantities, the velocity field and wave run-up on the sphere are also compared to those predicted by WAMIT.

Table 3 Surge response amplitudes (m/m) for the fine mesh and differences with respect to WAMIT results for the sphere

SURGE RAO (m/m)							
ω (rad/s)	WAMIT	Spline degree			Difference (%)		
		0	1	2	0	1	2
2.426	0.694	0.694	0.691	0.692	0.07	0.47	0.30
2.621	0.645	0.645	0.642	0.643	0.08	0.55	0.39
2.801	0.597	0.596	0.593	0.594	0.19	0.76	0.61
2.971	0.552	0.554	0.550	0.550	0.28	0.43	0.31
3.132	0.509	0.512	0.508	0.508	0.61	0.25	0.20
3.285	0.468	0.473	0.468	0.468	1.02	0.15	0.16
3.431	0.431	0.438	0.431	0.431	1.71	0.19	0.03
3.571	0.396	0.406	0.397	0.396	2.58	0.48	0.22
3.706	0.363	0.375	0.366	0.365	3.23	0.78	0.32
3.836	0.334	0.346	0.336	0.334	3.72	0.80	0.11
3.962	0.307	0.321	0.308	0.306	4.61	0.44	0.11
4.084	0.282	0.295	0.281	0.279	4.71	0.27	1.16
4.202	0.260	0.273	0.258	0.255	5.32	0.73	1.90
				Mean	2.16	0.49	0.45

Table 4 Heave response amplitudes (m/m) for the fine mesh and differences with respect to WAMIT results for the sphere

HEAVE RAO (m/m)							
ω (rad/s)	WAMIT	Spline degree			Difference (%)		
		0	1	2	0	1	2
2.426	1.185	1.181	1.188	1.184	0.35	0.60	0.32
2.621	1.304	1.295	1.307	1.301	0.67	0.93	0.46
2.801	1.479	1.458	1.476	1.466	1.47	1.25	0.65
2.971	1.712	1.688	1.714	1.698	1.39	1.51	0.94
3.132	1.887	1.870	1.887	1.864	0.87	0.92	1.23
3.285	1.726	1.787	1.749	1.739	3.56	2.14	0.60
3.431	1.301	1.390	1.337	1.340	6.84	3.79	0.22
3.571	0.927	0.960	0.929	0.936	3.49	3.19	0.75
3.706	0.673	0.679	0.653	0.669	0.88	3.73	2.45
3.836	0.504	0.493	0.479	0.493	2.25	2.83	2.83
3.962	0.390	0.373	0.360	0.374	4.36	3.43	3.89
4.084	0.309	0.292	0.290	0.301	5.56	0.60	4.01
4.202	0.250	0.233	0.242	0.249	6.43	3.68	2.83
				Mean	2.93	2.20	1.63

Fig. 15 Example of free-surface elevation for a point upstream and close to the hemisphere surface for $\omega = 4$ rad/s

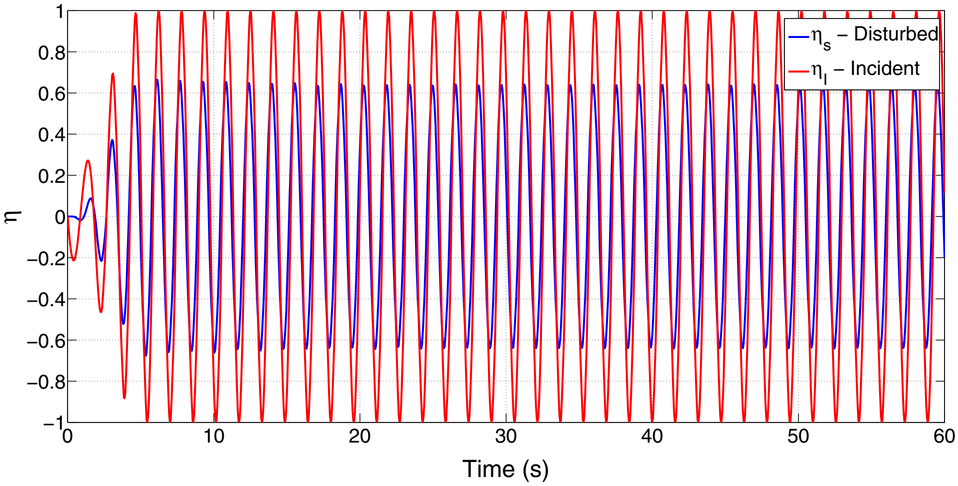

6.1 First-order response operator

The response amplitude operators (RAOs) were computed for a hemisphere of radius 1 m built with two patches and a circular free surface of radius 20 m defined by a single patch, as illustrated in Fig. 10.

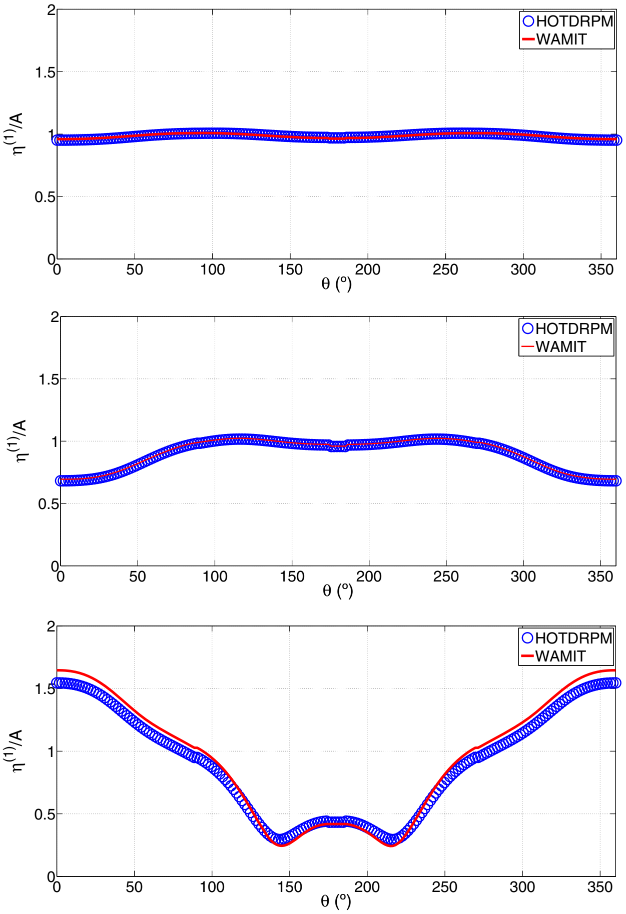

Fig. 16 Wave Run-up for the fixed hemisphere considering $\omega = 2$ rad/s (top) $\omega = 3$ rad/s (middle), $\omega = 4$ rad/s (bottom)

The convergence of the HOTDRPM code is studied considering three different meshes for both the floating body and free surface. For each mesh configuration, three spline degrees are studied in the solution approximation (0, 1, and 2) to provide an initial idea of the convergence rate. It should be recalled that in the present code, the geometry is always described in an NURBS pattern, even for zero-order degree, and therefore, the zero-order solution is not exactly a conventional low-order approximation. The main parameters for the three different meshes are given in Table 2 and the subdivisions in the physical space can be observed and compared in Fig. 11.

Figure 12 illustrates the time series of motions obtained with the time-domain code for surge and heave. The wave heading chosen was zero degrees, and thus, no sway, roll, or yaw motions are expected due to symmetry. Moreover, since the center of gravity was defined coincident to the geometric center, also no pitch response is expected.

Time series are then post-processed to obtain the amplitude of the response in the steady state. In this process, the first cycles of motion subjected to ramp and transient effects are discarded. The amplitudes are defined as the mean value of the several maxima and minima for the steady period.

The surge and heave RAOs obtained with both codes can be seen in Figs. 13 and 14, respectively. Good agreement is observed for the finest mesh regardless the spline degree. The coarser meshes present somewhat larger discrepancies for the zero- and first-order splines, which are more evident for the heave amplitude operator.

The effect of the spline degree on the surge and heave responses computed with the fine mesh can be assessed in Tables 3 and 4, respectively. These tables present the mean

Table 5 Comparison of HOTDRPM and WAMIT results regarding the wave run-up for a floating sphere

ω (rad/s)	Maximum			Minimum			Mean
	HOTDRPM	WAMIT	Difference (%)	HOTDRPM	WAMIT	Difference (%)	Difference (m)
2.0	1.01	1.01	1.49	0.95	0.96	0.80	0.00
2.2	1.01	1.01	1.69	0.92	0.94	0.17	0.01
2.4	1.02	1.02	3.15	0.87	0.89	0.23	0.01
2.6	1.02	1.03	3.90	0.81	0.83	1.19	0.01
2.8	1.02	1.02	3.40	0.68	0.69	0.12	0.01
3.0	0.99	1.00	3.70	0.53	0.52	0.16	0.01
3.2	0.92	0.89	3.58	0.49	0.46	1.01	0.07
3.4	1.23	1.35	4.59	0.47	0.38	2.12	0.09
3.6	1.45	1.54	4.73	0.35	0.29	0.05	0.07
3.8	1.55	1.65	6.40	0.29	0.24	4.21	0.07
4.0	1.61	1.73	6.62	0.29	0.22	7.12	0.07

differences between the results obtained with HOTDRPM and WAMIT. It can be seen that differences are lower for degree 2 compared to the first- and zero-order ones. In fact, all results were in good agreement, since the mean difference is less than 2.5%, and can be considered negligible for practical applications. As expected, the largest differences are related to low period (high frequency) waves, for the wavelength is smaller and the effect of free-surface discretization in the numerical solution is more pronounced.

6.2 Wave run-up on a floating sphere

One of the major contributions to the second-order drift forces comes from the line integral of the relative free-surface elevation over the body waterline. Therefore, to evaluate the accuracy associated to this integration, the wave run-up was computed for a range of frequencies from $\omega = 2$ rad/s to $\omega = 4$ rad/s with increments of 0.2 rad/s.

The free-surface integral along the waterline considers the shadow effect downstream, which means that the comparison must be performed for the entire waterline, assuming a collection of 200 grid points, where $\theta = 0°$ is upstream and $\theta = 180°$ is located downstream. As discussed before, the elevations are computed with a tolerance of 0.01 m (1% of sphere radius), so the points are located in a circle of radius $R = 1.01$ m. This should not influence the results appreciably, since the wavelength is always considerably larger than this value (varying from 3.85 to 15.41 m). A B-spline of degree 2 and the fine mesh were used in the computations for both body and free-surface patches, a combination that proved to be sufficiently accurate for the motion RAOs.

An example of the time series of free-surface elevation can be seen in Fig. 15 for the point located in ($x = 1.01$, $y = 0$), upstream of the flow, for $\omega = 4$ rad/s. In these results, η_I stands for the incident wave elevation and η_S corresponds to the disturbed field due to the presence of the body. The run-up (or rundown) free-surface elevation amplification factor is computed using Eq. (72), assuming an incident amplitude A_I. Here, t_{cut} is an initial cut off in the signal to avoid transient and impulsive effects and t_{sim} is the simulation time:

$$\frac{|\eta_i|}{A_I} = \frac{\sqrt{2}}{A_I}\left[\frac{1}{(t_{\text{sim}} - t_{\text{cut}})}\int_{t_{\text{cut}}}^{t_{\text{sim}}} \eta_i^2 \mathrm{d}t\right]^{1/2}, \quad i = 1, 2, \ldots N_p. \tag{72}$$

The comparison between HOTDRPM and WAMIT results is shown in Fig. 16 for three wave frequencies ($\omega = 2$ rad/s, $\omega = 3$ rad/s, and $\omega = 4$ rad/s). One may observe that for long waves (low frequency), the diffraction effects are not so relevant, since the waves are appreciably larger than the sphere radius. On the other hand, for short waves, the diffraction effects are very important and the amplification factor reaches values up to 60% of the incident wave amplitude. The agreement between the different methods is considered reasonable, and trends with wave frequency are captured properly. The more significant discrepancies occur for the shorter waves close to 0°, something that is justified by a "patch edge" effect for both free surface and sphere, since no continuity is imposed, as discussed previously. The influence of the topology of the patches can also be verified near singular points in the region close to the 0°, 90°, 180°, and 270° for both WAMIT and Rankine results, where a "jump" in the solution occurs. Moreover, for higher frequencies (close to 3.0 rad/s), it must be recalled that the body is close to its heave resonance, and since no additional external damping is being considered, vertical motions are quite amplified

Fig. 17 Velocity field for the floating hemisphere considering ω=2rad/s (top) ω=3rad/s (middle), ω=4rad/s (bottom)

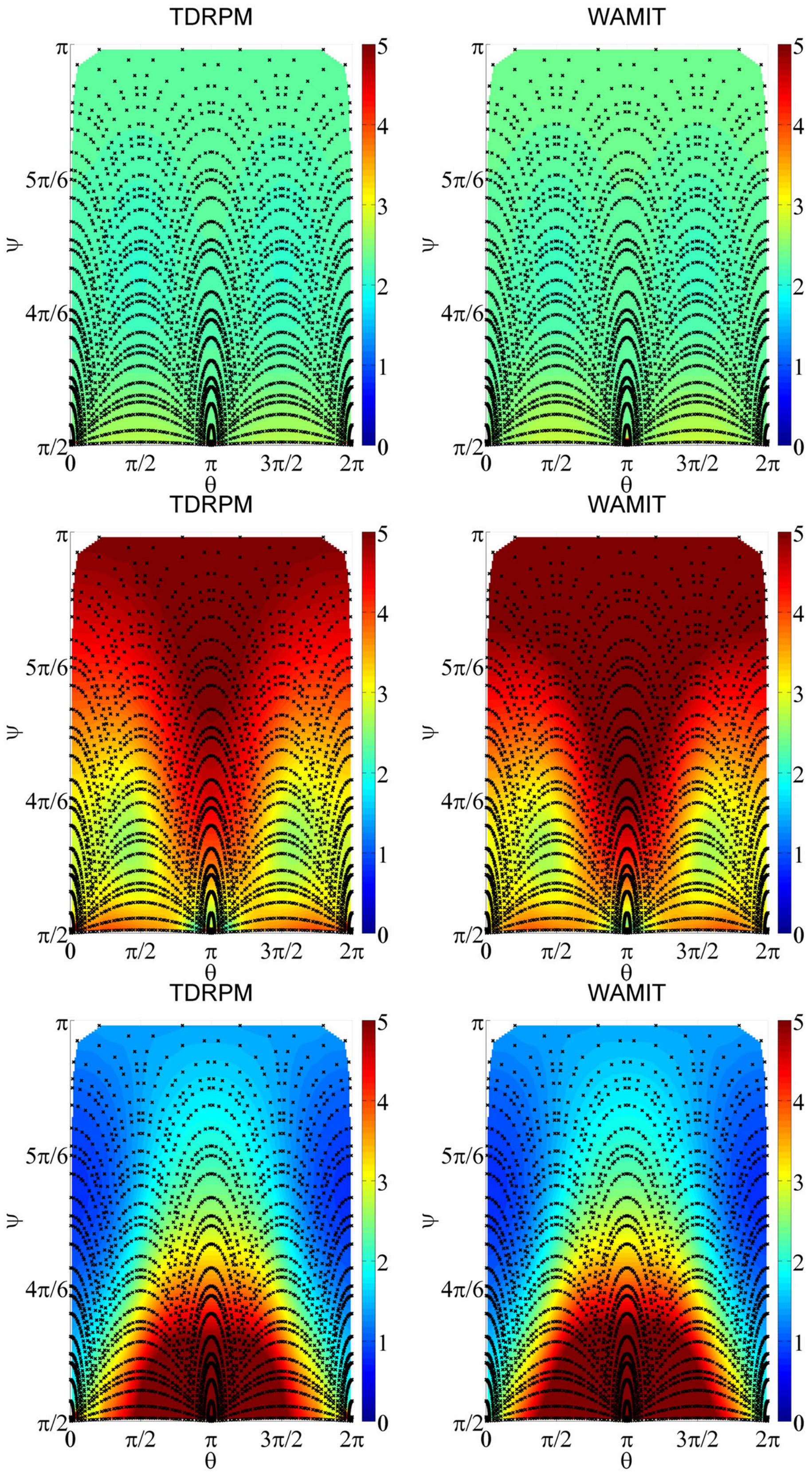

Table 6 Mean and standard deviation of the difference of the velocity field regarding WAMIT and HOTDRPM simulations for a floating sphere

ω (rad/s)	Mean diff V_x	Std diff V_x	Mean diff V_y	Std diff V_y	Mean diff V_z	Std diff V_z
2.0	0.02	0.01	0.02	0.07	0.02	0.06
2.2	0.02	0.01	0.02	0.06	0.01	0.06
2.4	0.02	0.01	0.01	0.06	0.00	0.05
2.6	0.03	0.01	0.01	0.05	0.00	0.05
2.8	0.04	0.01	0.01	0.06	0.00	0.05
3.0	0.05	0.01	0.02	0.06	0.01	0.06
3.2	0.03	0.02	0.04	0.07	0.03	0.06
3.4	0.01	0.01	0.03	0.07	0.02	0.06
3.6	0.01	0.01	0.01	0.06	0.01	0.06
3.8	0.01	0.01	0.01	0.06	0.01	0.06
4.0	0.00	0.01	0.01	0.06	0.02	0.06

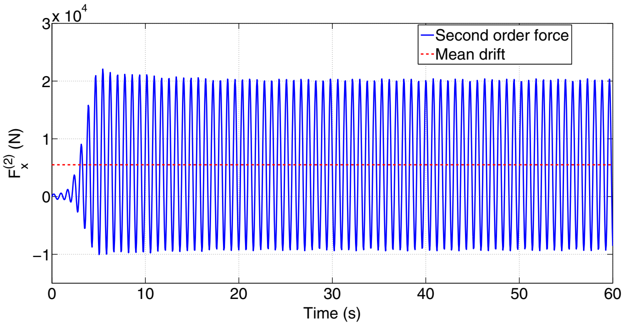

Fig. 18 Example of the surge quadratic second-order forces for a monochromatic wave for a fixed hemisphere $\omega = 4$ rad/s

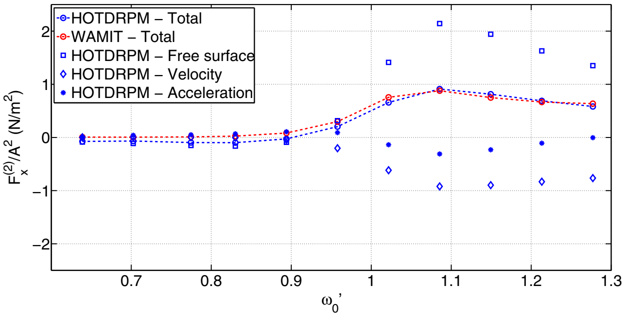

Fig. 19 WAMIT and HOTDRPM mean drift forces comparison in surge direction for a floating hemisphere. The run-up and velocity field components obtained from Rankine computations are also present

(see Fig. 14). In this condition, even small differences in the body motions may lead to appreciable variations in the wave run-up. Table 5 presents a comparison of the differences obtained in the run-up predictions according to the HOTDRPM and WAMIT for the several wave frequencies tested. Mean differences represent the mean value for the amplification factors measured in the 200 points of the waterline.

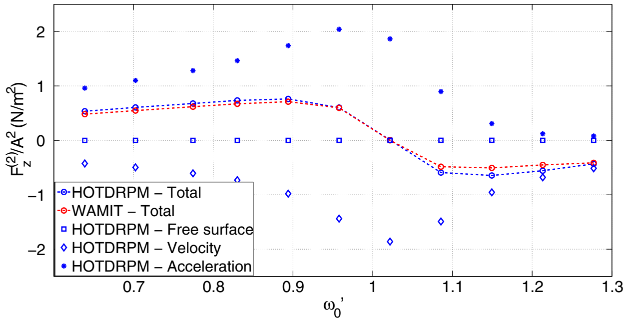

Fig. 20 WAMIT and HOTDRPM mean drift forces comparison in heave direction for a floating hemisphere

6.3 Velocity field for a floating sphere

The analysis regarding the accuracy of the velocity field is performed on the entire body surface, as required in the velocity integration process during the computation of the second-order drift forces.

The points are generated in the parametric space assuming 16 Gaussian points per higher order panel and a visual comparison of the variation of the velocity amplitude over the wetted surface predicted by both methods is given in Fig. 17 for $\omega = 2$ rad/s, $\omega = 3$ rad/s, $\omega = 4$ rad/s, following the polar coordinates defined in Eq. (73):

$$\begin{aligned} x &= R\cos(\theta)\sin(\psi) \\ y &= R\sin(\theta)\sin(\psi) \\ z &= R\cos(\psi) \\ 0 &\le \theta \le 2\pi\ ,\ \ \pi/2 \le \psi \le \pi. \end{aligned} \tag{73}$$

Table 6 presents a quantitative comparison of differences between both predictions considering mean and standard deviation values derived according to Eq. (74). Here, N_p is total number of points, $V_{xi\mathrm{TDRPM}}$ is the velocity amplitude value computed by the HOTDRPM code in point i, and $V_{xi\mathrm{WAMIT}}$ is the same computation performed using WAMIT:

Fig. 21 Example of surge force time series for two regular wave components (total, second order and first order—up to down)

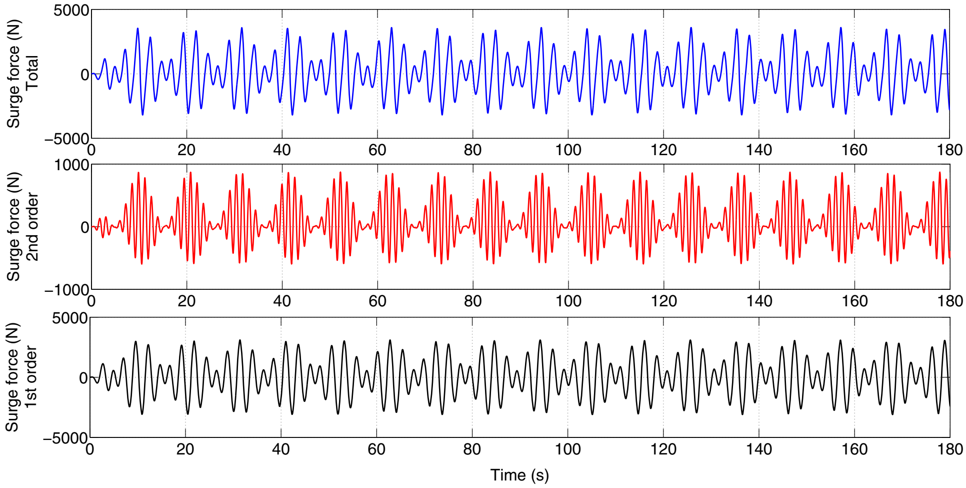

Fig. 22 Force spectrum considering two regular waves

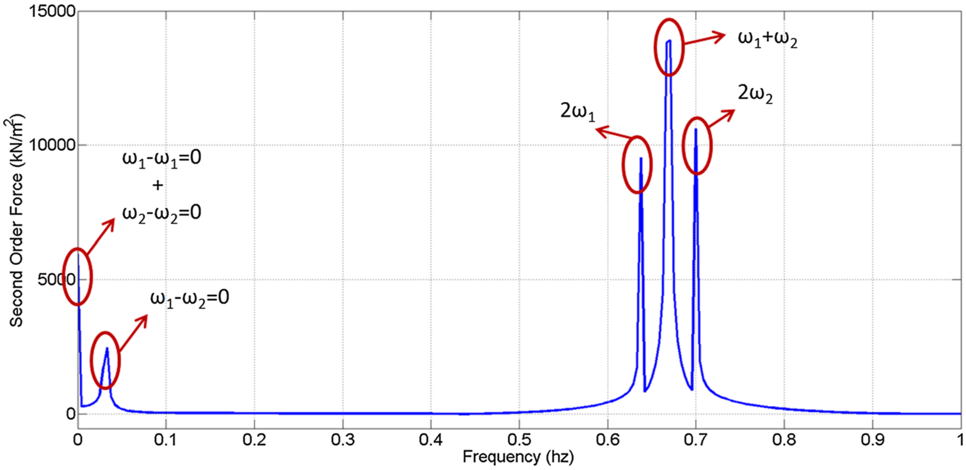

$$\mathrm{Meandiff}V_x = \frac{1}{N_p}\frac{\sum_{i=1}^{N_p}\left|V_{xi\mathrm{TDRPM}} - V_{xi\mathrm{WAMIT}}\right|}{A\omega}$$
$$\mathrm{Stddiff}V_x = \frac{1}{A\omega}\sqrt{\frac{\sum_{i=1}^{N_p}\left(V_{xi\mathrm{TDRPM}} - V_{xi\mathrm{WAMIT}}\right)^2}{N_p - 1}}. \qquad (74)$$

6.4 Mean drift forces for a floating sphere

This section presents an assessment of the mean drift forces computed by the time-domain method. In this analysis, the results are based on the simulation of regular (monochromatic) waves from which the loads on the sphere are obtained. An example of a time series of the second-order (quadratic) surge load for the fixed sphere is presented in Fig. 18.

It should be noticed that in time-domain simulations of regular waves, the second-order loads include two components with different frequencies, $\Delta\omega = 0$ (mean drift) and $\Delta\omega = 2\omega$ (double frequency). In the present section, only the mean drift component ($\Delta\omega = 0$) is addressed. It can be derived in a straightforward manner, by taking the mean value of the force time series (once again, the first cycles of simulations are discarded to avoid transient effects), following the procedure, as shown in Eq. (75):

$$\bar{F}_{x,z} = \frac{1}{\Delta t}\int_{t_i}^{t_i+\Delta t} F_{x,z}^{(2)}(t)\mathrm{d}t. \qquad (75)$$

The values obtained for the mean drift forces in surge and heave are then compared to WAMIT predictions. The agreement of the results can be assessed from the results in Figs. 19 and 20, respectively, for surge and heave.

The force components that contribute to the total mean drift force can be grouped in five different terms, following the proposal made by Pinkster [43]. Since no rotations are present for the sphere, only three of these components are not null, which are those expressed in Eqs. (76), (77), and (78). For an assessment of the magnitude of the different contributions, Figs. 19 and 20 also present the values computed for each one of the three terms.

Table 7 Comparison of quadratic second-order forces computed for both Rankine and WAMIT numerical methods in surge direction

Second-order surge forces

ID	ω_1	ω_2	$\frac{F_1^{(2)}(\omega_1-\omega_2)}{A_1A_2}$		$\frac{F_1^{(2)}(\omega_1+\omega_2)}{A_1A_2}$		$\frac{F_1^{(2)}(2\omega_1)}{A_1^2}$		$\frac{F_1^{(2)}(2\omega_2)}{A_2^2}$	
			Rank	WAMIT	Rank	WAMIT	Rank	WAMIT	Rank	WAMIT
1	2.00	2.20	1367.3	1292.6	10492.3	10210.1	9385.4	9601.9	10879.8	10749.7
2	2.00	2.61	2246.1	2392.3	10235.3	11143.3	9435.4	9601.9	12676.0	12187.1
3	2.20	2.80	2647.3	2824.2	12228.5	12228.5	10913.8	10749.7	12506.5	12408.2
4	2.61	2.80	3126.7	3257.0	13546.9	13546.9	13351.5	12187.1	13272.8	12408.2
5	2.00	3.00	2927.6	3324.4	10318.2	10318.2	9463.7	9601.9	12066.5	12450.7
6	2.00	2.80	2446.5	2905.1	11986.4	11986.4	9373.4	9601.9	12478.6	12408.2
7	2.00	3.20	3608.0	3624.6	10234.9	10234.9	9570.0	9601.9	11760.0	12601.9
8	2.20	2.61	1562.2	1351.1	11794.8	11794.8	10830.0	10749.7	12385.4	12187.1

Table 8 Comparison of quadratic second-order forces computed for both Rankine and WAMIT numerical methods in heave direction

Second-order heave forces

ID	ω_1	ω_2	$\frac{F_3^{(2)}(\omega_1-\omega_2)}{A_1A_2}$		$\frac{F_3^{(2)}(\omega_1+\omega_2)}{A_1A_2}$		$\frac{F_3^{(2)}(2\omega_1)}{A_1^2}$		$\frac{F_3^{(2)}(2\omega_2)}{A_2^2}$	
			Rank	WAMIT	Rank	WAMIT	Rank	WAMIT	Rank	WAMIT
1	2.00	2.20	5218.1	4857.3	2669.1	2785.4	2444.0	2587.8	3055.0	2998.8
2	2.00	2.61	4853.4	4987.1	2885.5	3015.4	2384.5	2587.8	3280.6	3529.0
3	2.20	2.80	5350.5	5201.3	3332.1	3249.7	2760.8	2998.8	3485.6	3538.3
4	2.61	2.80	6069.7	5578.1	3195.4	3533.1	3366.5	3529.0	3477.9	3538.3
5	2.00	3.00	4974.6	4687.6	2885.0	2928.6	2634.6	2587.8	3454.9	3336.8
6	2.00	2.80	5150.7	4889.5	2673.1	3014.8	2633.3	2587.8	3425.9	3538.3
7	2.00	3.20	4657.2	4402.9	2793.7	2765.6	2628.3	2587.8	3127.6	2936.6
8	2.20	2.61	5604.4	5276.7	3128.1	3249.2	2776.4	2998.8	3382.8	3529.0

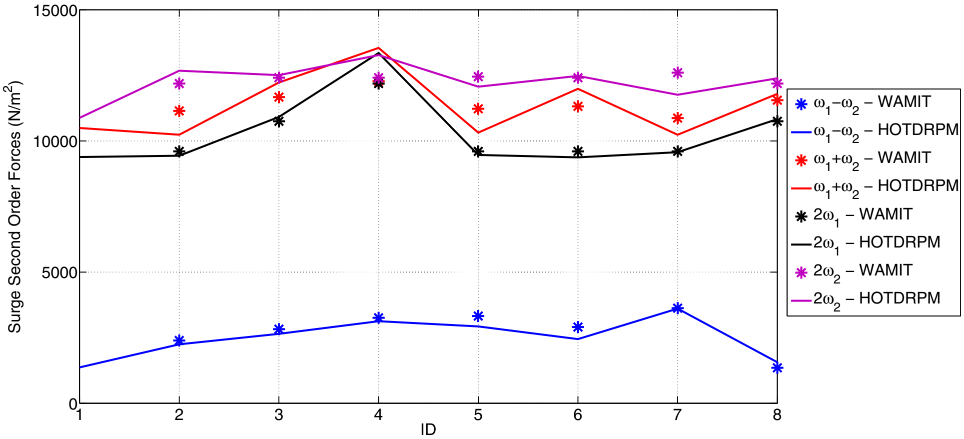

Fig. 23 Comparison between HOTDRPM and WAMIT results for quadratic transfer function for surge forces in both difference and sum frequencies

One may realize that all the three components are indeed important for the mean drift surge forces, whereas only the second and third components are relevant for heave:

$$F_1 = -\frac{1}{2}\rho g \oint_{WL} [\eta^{(1)} - (z_G^{(1)} + (y_Q - y_G^{(0)})\alpha^{(1)} - (x_Q - x_G^{(0)})\alpha^{(2)})]^2 \mathbf{n}^{(0)} \mathrm{d}l \Rightarrow \text{Freesurface} \tag{76}$$

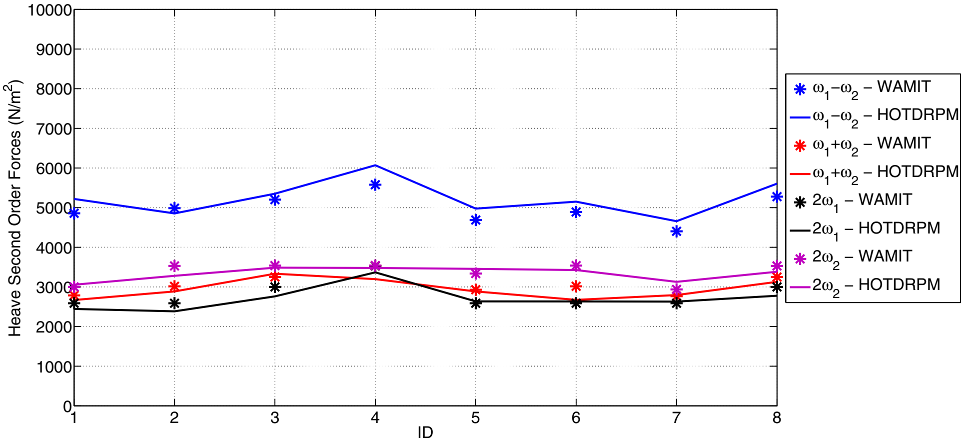

Fig. 24 Comparison between HOTDRPM and WAMIT results for quadratic transfer function for heave forces in both difference and sum frequencies

$$F_2 = \frac{1}{2}\rho \iint_{\bar{S}_B} \nabla\varphi^{(1)} \cdot \nabla\varphi^{(1)}\mathbf{n}^{(0)}\mathrm{d}S_B \Rightarrow \text{Velocity} \tag{77}$$

$$F_3 = \rho \iint_{\bar{S}_B} \mathbf{x}_Q^{(1)} \cdot \nabla\left(\frac{\partial\varphi_Q^{(1)}}{\partial t}\right)\mathbf{n}^{(0)}\mathrm{d}S_B \Rightarrow \text{Acceleration.} \tag{78}$$

Overall good agreement is observed for the results of both methods. Indeed, differences are less than 5 and 10% for heave and surge forces, respectively.

6.5 Sum- and difference-frequency second-order forces for a fixed sphere

The analysis of the quadratic sum and difference-frequency forces is based on simulations that consider the superposition of two or more regular wave components, thus providing several combinations of frequencies corresponding to the several quadratic wave interactions that are present.

As already mentioned for the case of the monochromatic wave, besides the desired sum and difference components, the computed loads also include the double frequency and zero (mean) values for each individual wave component. In fact, this is an important difference when compared to the conventional frequency-domain approach. In the latter, the desired frequency combinations must be defined previously and each combination is evaluated separately, whereas in the time-domain approach, all possible combinations will be included in the time series of loads, with the corresponding phases of the components.

An example of time series for the surge force (considering both first- and second-order loads) obtained in the simulation of a bichromatic wave can be seen in Fig. 21, in which the first- and second-order components are also presented separately for illustration purposes. The Fourier analysis of the second-order force signal is presented in Fig. 22.

In the case of two regular waves, there are five force components: the double frequencies ($2\omega_1$, $2\omega_2$) of the first and second components, the sum of frequencies ($\omega_1 + \omega_2$), the difference of components ($|\omega_1 - \omega_2|$), and the mean forces ($\omega_1 - \omega_1$ and $\omega_2 - \omega_2$). If three regular wave components were considered, ten different force components would be present. Regarding the mean drift, it should be observed that in the time-domain approach, it is computed considering the contribution of the regular components combined, and therefore, their individual contributions cannot be split into this analysis.

The comparison concerning the results of second-order loads for the double, sum, and differences frequencies for both surge and heave is shown in Tables 7 and 8, and are also presented graphically in Figs. 23 and 24. The comparisons are performed considering only the quadratic terms computed by WAMIT, thus neglecting any eventual contribution of the second-order potential. As for the mean drifts, a reasonable agreement is observed for all the combinations of frequencies tested.

Therefore, although numerical inaccuracies are present in the computation of some of the local quantities, particularly in the computation of the velocity field on the body surface, the results obtained for the hemisphere indicate that such inaccuracies do not compromise the evaluation of the integral values of the second-order loads, both for difference- and sum-frequency components. Moreover, the good agreement observed with WAMIT results attest the consistency of the algorithms adopted in the present version of the time-domain code.

7 Conclusions

The BEM computational solution of the wave–structure interaction problem was addressed in the scope of a multiscale approach. In this solution, hydrodynamic forces up to second order of magnitude are computed, except for the influence of the second-order potential. Such computations require the evaluation of the velocity field on the body surface, and thus, the accuracy obtained in the computation of the tangential derivatives of the potential function is important. For coping with this problem, a higher order approach was adopted, in which the body geometry is described by NURBS and the quantities in the panels by means of B-splines.

In the low-order panel method, the variables are the potential (velocities, pressure, free-surface elevation, etc.) in each element and the boundary conditions are applied in the collocation points of the panels providing a determined linear system. On the other hand, in the higher order approach the variables are the spline coefficients. Therefore, the imposition of the boundary conditions in the collocation points provides an undetermined system, motivating the definition of additional points. In the present development, the utilization of four collocation points per panel leads to an overdetermined system, solved (as the ordinary differential equations in the free surface) by means of a least square approach.

Many details on the algorithms required to perform the computational solution were presented and discussed along the paper, highlighting the problems that may arise when choosing between alternative numerical procedures.

For verifying the consistency of the numerical method, a simple body geometry consisting in a floating hemisphere was adopted as a case study. Steady-state results obtained in simulations performed with the higher order time-domain method were compared to those provided by the well-known frequency-domain code WAMIT.

First-order results, including motion response amplitude operators, velocity field, and wave run-up on the body surface were computed for the floating sphere by means of simulations of monochromatic waves. Comparisons attested a fine agreement between the results of both methods, although in a few points close to patch transitions or edges, the wave run-up and particularly the flow velocities are somewhat inaccurate.

Quadratic second-order loads, including sum and difference–frequency components, were analysed from simulations of bichromatic waves. Results showed a very good agreement with the second-order quantities computed by WAMIT, attesting that the localized numerical problems observed in the computation of the first-order velocity field do not compromise the accuracy of the second-order loads.

The development of the numerical method continues, and the next step regards the evaluation of the second-order potential. From the computational point of view, however, this is a quite demanding task and a previous check concerning the consistency of the algorithms addressed in this stage was imperative before moving to this next step. Inclusion of the effects of small current velocities is also planned as a future stage of the development.

Acknowledgements Felipe Ruggeri and Rafael Watai are thankful to the State of São Paulo Research Foundation, FAPESP, for providing their respective scholarship Grants (2012/06681-7) and (2010/08778-2). Alexandre Simos acknowledges the Brazilian National Research Council, CNPq, for his research grant. Authors are wish to thank Petrobras for supporting the previous work on the low-order TDRPM code, which actually motivated the present development.

References

1. ANSYS (2009) AQWA LINE MANUAL—Release 12.0
2. Babarit A, Delhommeau G (2015) Theoretical and numerical aspects of the open source bem solver nemoh. In: Proceedings of the 11th European wave and tidal energy conference (EWTEC2015)
3. Bandyk PJ, Beck RF (2011) The acceleration potential in fluid-body interaction problems. J Eng Math 70:147–163. https://doi.org/10.1007/s10665-010-9446-0
4. COMPASS (2015). http://www.compassis.com/compass/en/productos/seafem. Internet page. Accessed 12 Apr 2015
5. Contento G (2000) Numerical wave tank computations of non-linear motions of two-dimensional arbitrary shaped free floating bodies. Ocean Eng 27(5):531–556. https://doi.org/10.1016/S0029-8018(98)00059-6
6. Cummins WE (1962) The impulse response function and ship motions. Tech. Rep. 1661, David Taylor Model Basin
7. van Daalen EFG (1993) Numerical and theoretical studies of water waves and floating bodies. Ph.D. thesis, University of Twente
8. Dombre E, Benoit M, Violeau D, Peyrard C, Grilli S (2015) Simulation of floating structure dynamics in waves by implicit coupling of a fully nonlinear potential flow model and a rigid body motion approach. J Ocean Eng Mar Energy 1(1):55–76. https://doi.org/10.1007/s40722-014-0006-y
9. Ferrant P (1996) Simulaton of strongly nonlinear wave generation and wave-body interactions using a 3-d mel model. In: Proceedings of 21st symposium on naval hydrodynamics. National Academy Press, pp 93–109
10. Ferrant P (1998) Fully nonlinear interactions of long-crested wave packets with a three-dimensional body. In: Proceeding of 22nd ONR symposium on naval hydrodynamics, Washington, USA
11. Ferrant P, Le Touze D, Pelletier K (2003) Non-linear time-domain models for irregular wave diffraction about offshore structures. Int J Numer Methods Fluids 43(10–11):1257–1277
12. Greco M (2001) A two-dimensional study of green-water loading. Ph.D. thesis, NTNU—Norwegian University of Science and Technology
13. Grilli ST, Subramanya R (1994) Quasi-singular integrations in the modelling of nonlinear water waves. Eng Anal Bound Elem 13(2):181–191. https://doi.org/10.1016/0955-7997(94)90020-5
14. Grilli ST, Subramanya R (1996) Numerical modeling of wave breaking induced by fixed or moving boundaries. Comput Mech 17(6):374–391. https://doi.org/10.1007/BF00363981
15. Grilli ST, Skourup J, Svendsen A (1989) An efficient boundary element method for nonlinear water waves. Eng Anal Bound Elem 6(2):97–107. https://doi.org/10.1016/0955-7997(89)90005-2
16. Grilli ST, Guyenne P, Dias F (2001) A fully non-linear model for three dimensional overturning waves over an arbitrary bottom. Int J Numer Methods Fluids 35(7):829–867. https://doi.org/10.1002/1097-0363(20010415)35:7%3c829::AID-FLD115%3e3.0.CO;2-2
17. Grilli ST, Dias F, Guyenne P, Fochesato C, Enet F (2010) Progress in fully nonlinear potential flow modeling of 3D extreme ocean waves, chap 3. Advances in Numerical Simulation of

Nonlinear Water Waves. World Scientific Publishing, pp 75–128. https://doi.org/10.1142/9789812836502-0003

18. Guerber E, Benoit M, Grilli S, Buvat C (2012) A fully nonlinear implicit model for wave interactions with submerged structures in forced or free motion. Eng Anal Bound Elem 36(7):1151–1163. https://doi.org/10.1016/j.enganabound.2012.02.005
19. Hass J, Farouki RT, Han CY, Song X, Sedeberg TW (2007) Guaranteed consistency of surface intersections and trimmed surfaces using a coupled topology resolution and domain decomposition scheme. Adv Comput Math 27(1):1–26. https://doi.org/10.1007/s10444-005-7539-5
20. IGES (1986) Initial Graphics Exchange Specification, Version 3.0, Document No. NBSIR 86-3359. Massachussets Institute of Technology
21. Israeli M, Orszag SA (1981) Approximation of radiation boundary conditions. J Comput Phys 41(1):115–135. https://doi.org/10.1016/0021-9991(81)90082-6
22. John F (1949) On the motion of floating bodies i. Pure Appl Math 2(1):13–57. https://doi.org/10.1002/cpa.3160020102
23. John F (1950) On the motion of floating bodies ii. Pure Appl Math 3(1):45–101. https://doi.org/10.1002/cpa.3160030106
24. Kim DJ, Kim MH (1997) Wave-current interaction with a large three-dimensional body by thobem. J Ship Res 41(4):273–285
25. Kim GD, Lee CS, Kerwin JE (2007) A b-spline based higher order panel method for analysis of steady flow around marine propellers. Ocean Eng 34(14–15):2045–2060. https://doi.org/10.1016/j.oceaneng.2007.02.013
26. Kim MH, Koo WC (2005) Numerical Models in Fluid-Strucutre Interaction, chap 2D. Fully nonlinear wave tanks. WIT Press, pp 43–81. ISBN 978-1-85312-837-0
27. Koo W (2003) Fully nonlinear wave-body interactions by a 2d potential numerical wave tank. Ph.D. thesis, Texas AM University
28. Koo W, Kim MH (2004) Freely floating-body simulation by a 2d fully nonlinear numerical wave tank. Ocean Eng 31(16):2011–2046. https://doi.org/10.1016/j.oceaneng.2004.05.003
29. Kring DC (1994) Time domain ship motions by a three-dimensional rankine panel method. Ph.D. thesis, Massachussets Institute of Technology
30. Kring DC, Milewski WM, Fine NE (2004) Validation of a nurbs-based bem for multihull ship seakeeping. In: 25th symposium of naval hydrodynamics
31. Lee CH, Newman JN (2005) Computation of wave effects using the panel method. WIT Transactions on State-of-the-art in Science and Engineering
32. Lin WM, Salvesen N (1997) Nonlinear time-domain simulation of ship capsizing in beam seas. Tech. rep, United States Coast Guard
33. Lin WM, Yue DKP (1991) Numerical solutions for large-amplitude ship motions in the time-domain. In: Proceedings of the 18th symposium in naval hydrodynamics, pp 41–66. https://doi.org/10.17226/1841
34. Lin WM, Yue DKP (1992) Wave forces on a surface-piercing sphere undergoing large amplitude motions. In: Proceedings of the seventh international workshop on water and floating bodies
35. Liu Y, Xue M, Yue DK (2001) Computations of fully nonlinear three dimensional wave-wave and wave-body interactions. Part 2. Nonlinear waves and forces on a body. J Fluid Mech 438:41–66. https://doi.org/10.1017/S0022112001004396
36. Liu YH, Kim CH, Lu XS (1991) Comparison of higher-order boundary element and constant panel methods for hydrodynamic loadings. Int J Offshore Polar Eng 1(1):8–16
37. Liu YH, Kim CH, Kim MH (1993) The computation of mean drift forces and wave run-up by higher-order boundary element method. Int J Offshore Polar Eng 3(2):101–106
38. Liu YH, Kim MH, Kim CH (1995) The computation of second-order mean and double-frequency wave loads on a compliant TLP by HOBEM. Int J Offshore Polar Eng 5(2):111–119
39. Maniar HD (1995) A three dimensional higher order panel method based on b-splines. Ph.D. thesis, MIT—Massachusset Institute of Technology
40. Matos V, Simos AN, Sphaier SH (2011) Second-order resonant heave, roll and pitch motions of a deep-draft semi-submersible: theoretical and experimental results. Ocean Eng 38:17–18
41. Nishimoto K, Fucatu CH, Masetti IQ (2002) Dynasim—a time domain simulator of anchored FPSO. J Offshore Mech Arct Eng. https://doi.org/10.1115/1.1513176
42. Piegl L, Tiller W (1997) The NURBS book, 2nd edn. Springer, Berlin (**ISBN 978-3-642-97385-7**)
43. Pinkster JA (1980) Low frequency second order wave exciting forces on floating structures. Ph.D. thesis, Delft University of Technology
44. Prins H (1995) Time-domain calculations of drift forces and moments. Ph.D. thesis
45. Ruggeri F (2012) A time domain rankine panel method for 2d seakeeping analysis. Thesis—University of Sao Paulo, MSc
46. Ruggeri F, Watai RA, Simos AN (2015) A higher order time domain rankine panel method for linear and weakly non-linear computation. In: Proceedings of the ASME 2015 34th international conference on ocean, offshore and arctic engineering. https://doi.org/10.1115/OMAE2015-42234
47. Shao YL (2010) Numerical potential-flow studies on weakly-nonlinear wave-body interactions with/without small forward speeds. Ph.D. thesis, NTNU—Norwegian University of Science and Technology
48. Tang CK, Medioni G (1998) Interference of integrated surface, curve and junction descriptions from sparse 3d data. IEEE Trans Pattern Anal Mach Intell 20(11):1206–1223
49. Tanizawa K (2000) The state of the art on numerical wave tank. In: Proceeding of 4th Osaka coloquium on seakeeping performance of ships, pp 99–114
50. Tanizawa K, Minami M, Naito S (1999) Estimation of wave drift force by a numerical wave tank. In: 9th international offshore and polar engineering conference
51. Tanizawa K, Minami M, Sawada H (2000) Estimation of wave drift force by a numerical wave tank, 2nd report. 10th international offshore and polar engineering conference
52. Teixeira FG, Creus GJ (2008) A robust algorithmn to determine surface/surface itersection in both parametric spaces. Mecánica Computacional XXVII:3093–3115
53. Vugts JH (1968) The hydrodynamic coefficients for swaying, heaving and rolling cylinders in a free surface. International Shipbuilding Progress, pp 251–275
54. WAMIT I (2014) Wamit User Manual Versions 6.4, 6.4s
55. Watai RA (2014) A time-domain boundary elements method for the seakeeping analysis of offshore systems. Ph.D. thesis, University of Sao Paulo
56. Wehausen JV, Laitone EV (1960) Surface waves. In: Truesdell C (ed) Fluid dynamics/Strömungsmechanik. Encyclopedia of physics/Handbuch der physik, vol 3/9. Springer, Berlin, pp 446–478
57. Wu G (2004) Direct simulation and deterministic prediction of large-scale nonlinear ocean wave-field. Ph.D. thesis, Massachussets Institute of Technology
58. Xue M, Xu H, Liu Y, Yue DKP (2001) Computations of fully nonlinear three-dimensional wave-wave and wave-body interactions. Part 1. Dynamics of steep three dimensional waves. J Fluid Dyn 438:11–39. https://doi.org/10.1017/S0022112001004396
59. Yan H (2010) Computations of fully nonlinear three-dimensional wave-body interactions. Ph.D. thesis, Massachussets Institute of Technology